Antarctic bioconstructional bryozoans from Terra Nova Bay (Ross Sea): morphology, skeletal structures and biomineralization.

Chiara Lombardi, Piotr Kuklinski, Edoardo Spirandelli, Giorgio Bruzzone, Giancarlo Raiteri, Andrea Bordone, Claudio Mazzoli, Matthias López Correa, Robert van Geldern, Laurent Plasseraud, et al.

minerals

MDPI

Article

Antarctic Bioconstructional Bryozoans from Terra Nova Bay (Ross Sea): Morphology, Skeletal Structures and Biomineralization

Chiara Lombardi [1,*], Piotr Kuklinski [2], Edoardo Spirandelli [3], Giorgio Bruzzone [3], Giancarlo Raiteri [1], Andrea Bordone [1], Claudio Mazzoli [4], Matthias López Correa [5,6], Robert van Geldern [6], Laurent Plasseraud [7], Jérôme Thomas [8] and Frédéric Marin [8]

1 Marine Environment Research Centre of S. Teresa, Italian National Agency for New Technologies, Energy and Sustainable Economic Development (ENEA), 19032 Lerici, Italy
2 Department of Marine Ecology, Institute of Oceanology, Polish Academy of Sciences, 81-712 Sopot, Poland
3 Institute of Marine Engineering, Italian National Research Council (CNR), 16149 Genova, Italy
4 Department of Geosciences, University of Padova, 35131 Padova, Italy
5 CNR-ISMAR, Via Gobetti 101, 40129 Bologna, Italy
6 GeoZentrum Nordbayern, Friedrich-Alexander-Universität Erlangen-Nürnberg, D-91054 Erlangen, Germany
7 Institute of Molecular Chemistry, ICMUB UMR CNRS 6302, University of Burgundy-Franche-Comté, 21078 Dijon, France
8 UMR CNRS 6282 Biogéosciences, Bâtiment des Sciences Gabriel, Université de Bourgogne-Franche-Comté (UBFC), 21000 Dijon, France
* Correspondence: chiara.lombardi@enea.it

Abstract: Among Antarctic bryozoans, some species are able to develop calcitic bioconstructions promoting habitat complexity, but the processes leading to biomineral formation are mostly unknown. The present work investigated three Antarctic bryozoans, from morphological to skeletal features, including the organic matrix associated with the skeleton (SOM). *Cellarinella nutti* Rogick, 1956 and *Reteporella frigida* Waters, 1904 were collected in November 2018 from a shallow site (25 m) and *Cellarinella njegovanae* Rogick, 1956 from a deep site (110 m) at Terra Nova Bay (Ross Sea, Antarctica). Both *Cellarinella* species showed 5–6 "growth check lines" (gcl) on their laminae. The morphometrical characterization conducted on the growth bands (gb) and zooids, within the band across bands, revealed a variability in length with time (*C. nutti*: from 4099 µm for gb1 to 1449 µm for gb6; *C. njegovanae*: from 1974 µm for gb 3 to 7127 µm for gb2). Zooid length varied within gb, from the proximal to the distal part of the bands, but differences also occurred across bands. The shortest zooids (~625 µm) were found at the proximal part and the longest (~ 1190 µm) in the middle part of the gb in *C. nutti*, whereas in *C. njegovanae* the shortest zooids (~ 660 µm) were found in the distal part and the longest (~1190 µm) in the proximal part of the gb. Micro-CT analyses indicated the ratio of basal zooidal walls (RbwT gcl/gb) ranged from 3.0 to 4.9 in *C. nutti* and from 2.3 to 5.9 in *C. njegovanae*, whereas *Reteporella frigida* did not form any gcl on either side of the colony. Preliminary characterizations of the SOM for the three species evidenced a mixture of proteins and polysaccharides with properties similar to those of better-known biominerals, in terms of quantity and electrophoretic behavior. In addition, a "lectin fingerprint" has been established for the first time in bryozoans, displaying the presence of chitin or chitin-related saccharides. Understanding the complexity of the processes regulating skeleton formation is a key aspect in comprehending the adaptation of bioconstructional ecosystems and the survival of the associated biodiversity under the future ocean.

Keywords: Bryozoa; Antarctica; calcifying ecosystem; growth check lines; zooid morphometrics; skeletal organic matrix (SOM); seawater stable isotopes; climate change

Citation: Lombardi, C.; Kuklinski, P.; Spirandelli, E.; Bruzzone, G.; Raiteri, G.; Bordone, A.; Mazzoli, C.; López Correa, M.; van Geldern, R.; Plasseraud, L.; et al. Antarctic Bioconstructional Bryozoans from Terra Nova Bay (Ross Sea): Morphology, Skeletal Structures and Biomineralization. *Minerals* **2023**, *13*, 246. https://doi.org/10.3390/min13020246

Academic Editor: Aleksey Sadekov

Received: 10 January 2023
Revised: 1 February 2023
Accepted: 6 February 2023
Published: 9 February 2023

1. Introduction

Bryozoans are sessile aquatic animals, formed by tens to thousands of modular genetically identical units (i.e., zooids) building extremely diverse colonies [1]. They are fairly ubiquitous across habitats, distributed from freshwater to marine environments, from shorelines to the deep sea, and from the tropics to polar oceans. The colonial body-plan of Bryozoa can be traced back to the early Cambrian (Age 3), coincident to their first occurrence of other major metazoan phyla [2]. Probably originating from a common colonial ancestor [3,4], bryozoan skeletal biomineralization evolved independently at least twice across two major bryozoan clades: the Stenolaemata during the Early Ordovician (or perhaps the Cambrian) and the Gymnolaemata (order Cheilostomata) in the Jurassic. The size of their colonies (cm to dm scale) and the biomineralized components enhanced bryozoan fossilization potential [1,5–7]. Most of the extant bryozoan species are marine and belong to two orders: Cyclostomata within the class Stenolaemata and Cheilostomata within the class Gymnolaemata. Both orders produce well-calcified skeletons and, as framework builders, provide habitats over timescales of years to decades [8].

Bryozoans utilize two polymorphs of calcium carbonate ($CaCO_3$), calcite and aragonite, for building their skeletons. Polymorph relative proportion shows a strong latitudinal gradient, especially in Cheilostomata [9]. At high latitudes (>60°, polar areas) calcitic species are dominant, and few bimineralic and no aragonitic species are found; at mid latitudes (30–60°), bimineralic species are very common, calcitic less-represented and aragonitic species are very rare; at low latitudes (<30°), aragonitic and bimineralic species outnumber calcitic species [6,9]. Calcifying bryozoans are able to build complex architectures including biogenic reefs [10], whose structures enhance rich associated-species assemblages that are highly diverse and taxonomically complex [8,11–13]. Processes facilitating biomineral formation in this taxon are mostly unknown despite the need to comprehend their evolution and to understand their vulnerability or resilience to fast-occurring changes, especially in polar regions.

Antarctica represents an important component of Earth's climate system, interacting with the rest of the planet through shared ocean, atmosphere, and ecological systems. Its footprint is critical considering the ocean surface occupied as well as its extensive permafrost and glaciated areas [14,15]. In particular, the Ross Sea is the center of the highest productivity of the Southern Ocean (SO) [16], determining global biogeochemical cycles and the sequestration of anthropogenic CO_2 into the deep ocean [17,18]. Over the next century, the effects of climate change on the continent and in the ocean are expected to exacerbate, especially in Antarctica [19]. Alterations in the SO driven by climate change are consequently impacting marine ecosystems and coastal environments. Such alterations include increased temperature and altered sea ice coverage, iceberg scour in benthic habitats, ocean acidification, salinity/freshening, and low oxygen levels [20–23]. Considering the global importance of the SO as an atmospheric carbon sink [15], any changes in its ecosystem characteristics will determine the future states of the oceans as a whole [22].

Among SO ecosystems, habitat-forming bryozoans [8] contribute to the extensive (>1000 km of coverage) and densely structured communities of the Weddell, the Lazarev [24], and the Ross seas [25]. Bryozoan diversity in the SO is estimated at more than 400 species, mostly of Cheilostomata and Cyclostomata [26–30], often dominating communities of Vulnerable Marine Ecosystems (VME) in the deep ocean [31]. Some of these bioconstructional species display changes in the length of autozooids and/or presence of ovicells (i.e., reproductive zooids with larval brooding chambers), as well as in zooidal wall thickness during skeletal growth. These changes produce characteristic growth check lines on the skeletons [32–34]. Such lines correspond to annual cessation or reduced growth over the winter period, and their formation is mainly attributed to limiting factors such as food availability and temperature [35]. Separating each year's growth, these lines have been used to determine colony age and have revealed slower growth in polar species compared to temperate species [36–38].

Even though the inorganic phase of bryozoan skeletons has been extensively studied in both fossil and recent species, the cellular mechanisms of biomineralization are still unknown. In particular, the molecules regulating the deposition of calcium carbonate and the genes responsible for the formation of the bryozoan skeleton are some of the basic topics that need to be addressed [6]. At cellular level, the cuticle (i.e., zooidal organic cover) underlain by epithelial cells seems to act as template for mineralization in bryozoans [6,38]. The epithelium secreting the mineral constituent of the zooid originates from a ring of generative cuboidal cells proximal to the palisade cell cap. These cells are accommodated within the surface layer by the movement of the generative zone and the palisade cell cap. The new epithelium first exudes the cuticle and then an irregularly electron-dense sheet, becoming the seeding surface for the first crystallites of the biomineralized skeleton [38]. Analogous to other skeleton-forming metazoans, bryozoans are believed to finely-tune the deposition of their skeletal biominerals via a complex array of secreted macromolecules [39,40] collectively constituting the skeletal organic matrix (SOM). However, unlike other calcifying metazoans, this matrix is totally unknown in bryozoans. In better-studied models, SOM is a mixture of proteins, peptides, polysaccharides and sometimes lipids and pigments, with proteins as the most prominent constituents. The SOM generally represents no more than 1% of the biomineralized structure (by weight). It becomes occluded in the calcified skeleton once formed. Because of its supposed ability to favor mineral nucleation, to control the shape of newly formed crystallites, and to organize them spatially in well-defined microstructures, the SOM and, in particular, its protein moieties have been the focus of several studies covering decades of research in biomineralization per se in several metazoans but not bryozoans [41].

For the present study, three Antarctic endemic species belonging to *Cellarinella* Waters, 1904 and *Reteporella* Busk, 1884 genera were collected in 2018 at Terra Nova Bay (Ross Sea, Antarctica), from a shallow site (25 m) and a deep site (110 m). These target organisms, forming bioconstructional ecosystems and playing an important role in carbon immobilization [13,20,42–44], were investigated at skeletal and cellular levels, with the overall aim being to characterize, for the first time in bryozoans, the macromolecules constituting the skeletal organic matrix (SOM). Specifically, we: (1) taxonomically determined the target species via morphological investigations; (2) analyzed the skeletal structures at zooidal (thickness of zooidal walls) and colonial levels (i.e., number and thickness of the growth check lines) using Micro-CT; (3) characterized, for the first time, the SOM in three bryozoans species, using various molecular techniques including SDS-PAGE, FT-IR, CHNS analysis and enzyme-linked lectin assay (ELLA); and (4) determined seawater isotopic composition and DIC at the shallow sampling site (25 m) rich in bioconstructional ecosystems.

2. Materials and Methods

2.1. Study Area, Biological and Seawater Collection

The study area is located in Terra Nova Bay (TNB) (Figure 1), at the southwestern edge of the Ross Sea (Antarctica). Characterized by a tortuous continental shelf with numerous banks and trenches, TNB extends for 80 km × 30 km and has a mean depth of about 450 m, with greater depths close to the coast and down to 1000 m depths in the near basin. Terra Nova Bay is delimited by the narrow peninsula of Cape Washington (74°44′ S 163°45′ E), on the northern side, and by the Drygalski Ice Tongue (64°43′ S 60°44′ W), arising from David Glacier, on the southern side. The peculiar orography determines the climate of the region, which consists of katabatic winds, which keep the area free of ice, causing temperature drops (surface seawater temperature range: −1.9, +1 °C) [45], and a delay in summer seawater stratification. These winds are also responsible for the formation and maintenance of *polynyas* (i.e., recurrent regions of open water with thin or reduced ice concentration) during wintertime [46]. In coastal areas, *polynyas* are generated by persistent wind-driven export of sea-ice causing continuous sea ice formation with consequent strong heat loss and salt injection [47].

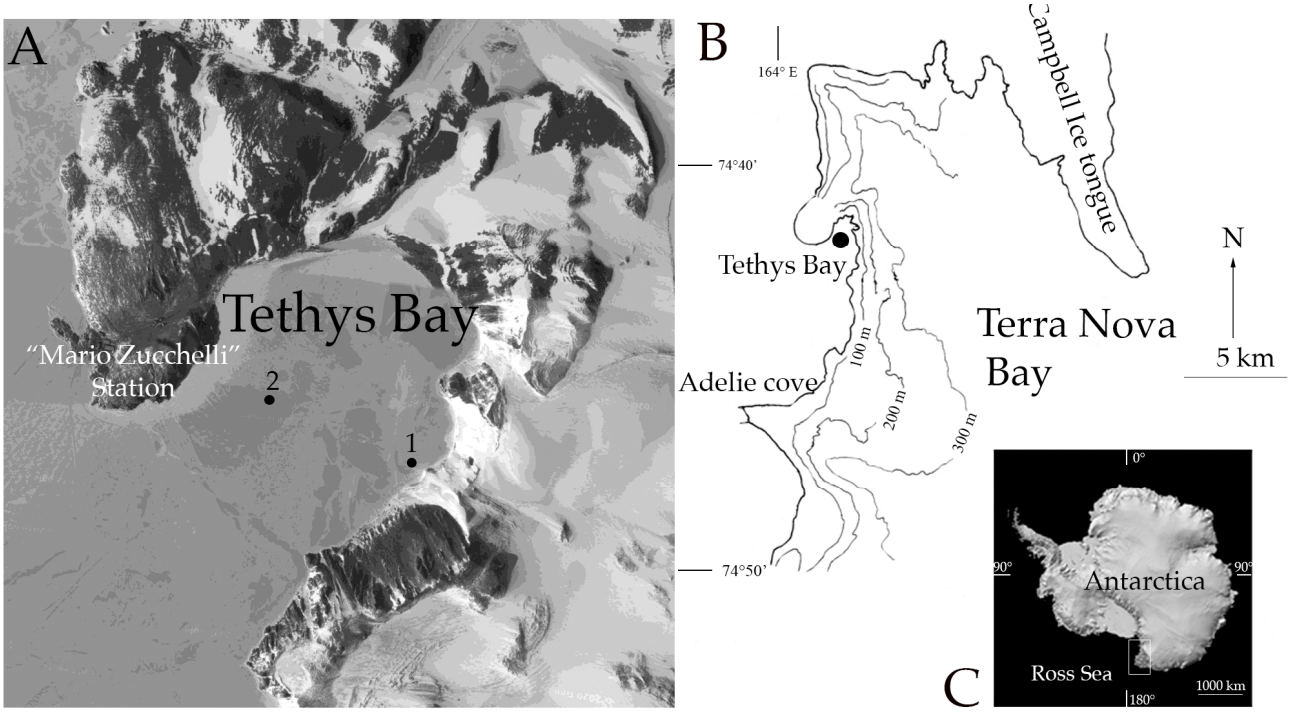

Figure 1. Study area and collection sites. (**A**) Zoomed view of Tethys Bay, (within Terra Nova Bay, Ross Sea), with the positions of the collection sites (1, 2) (modified from Google Earth); (**B**) Map of Terra Nova Bay; (**C**) Antarctica (modified from Geopolar geospatial Centre).

The bay is entirely covered by sea ice for at least 9 months of the year [48], which highly impacts the cycling of chemical and biological processes and limits CO_2 exchanges between air and sea. Such limits in the equilibrium of Antarctic surface water with the overlying atmosphere determine supersaturation with respect to CO_2, and under saturation with respect to the DO of the surface seawater. In the study site, the variability of the surface carbonate system properties has been observed to be primarily controlled by biological activities [49,50]. When the ice melts, phytoplankton blooms greatly affect the carbonate system and the local productivity of the benthic ecosystems. Furthermore, the changes in species composition depend on sea ice influence, current, and water mixing [51], as well as physiological processes of the bacteria present [52]. On a macro scale, benthic ecosystems containing calcifying suspension feeders such as bryozoans, corals, sponges, molluscs, and echinoderms [50,53,54], contribute to the environmental changes through their physiological activities (i.e., respiration, photosynthesis, calcification). Food availability occurring a few hours after ice melting allows these consumers to adopt a more specialized diet and an increased feeding rate [50,53,55,56]. Given the abundance of calcifiers, the reduction of DO, pCO_2, and saturation state at the site [13] has been related to the intensification of their physiological activities. These include feeding, but also growth through biomineralization processes (i.e., carbonate sequestration), and also reproductive activities in the summer months [57,58].

Three species of bioconstructional bryozoans were collected during the XXXIV Italian Expedition to Antarctica, in November 2018, from two sites. *Reteporella* sp. and *Cellarinella* sp.1 were collected at Site 1 (coordinates: 74°40.537′ S , 164°04.169′ E) (Figure 1) at 25 m depth by means of scuba diving (Figure 2) from the ice-pack, whereas *Cellarinella* sp.2 was collected at Site 2 (coordinates: 74°41.371′ S, 164°06.275′ E) (Figure 1) at 110 m depth, by using a remotely operated underwater vehicle (ROV) (Figure 2). Once collected, all specimens were placed in thermic boxes and transported to "Mario Zucchelli Station". From Site 1, at 25 m depth, four replicate seawater samples were collected by using a Niskin bottle deployed from the ice-pack, together with one conductivity–temperature–depth

probe (CTD, SBE37-SMP-ODO, SEA-BIRD, Bellevue, WA, USA) and one pH meter SeaFET (SeaFET V2, SEA-BIRD, Bellevue, WA, USA). After the sampling, samples were poisoned with mercuric chloride solution and kept cool at +4 °C. From Site 2 (110 m) seawater sample collection was not possible.

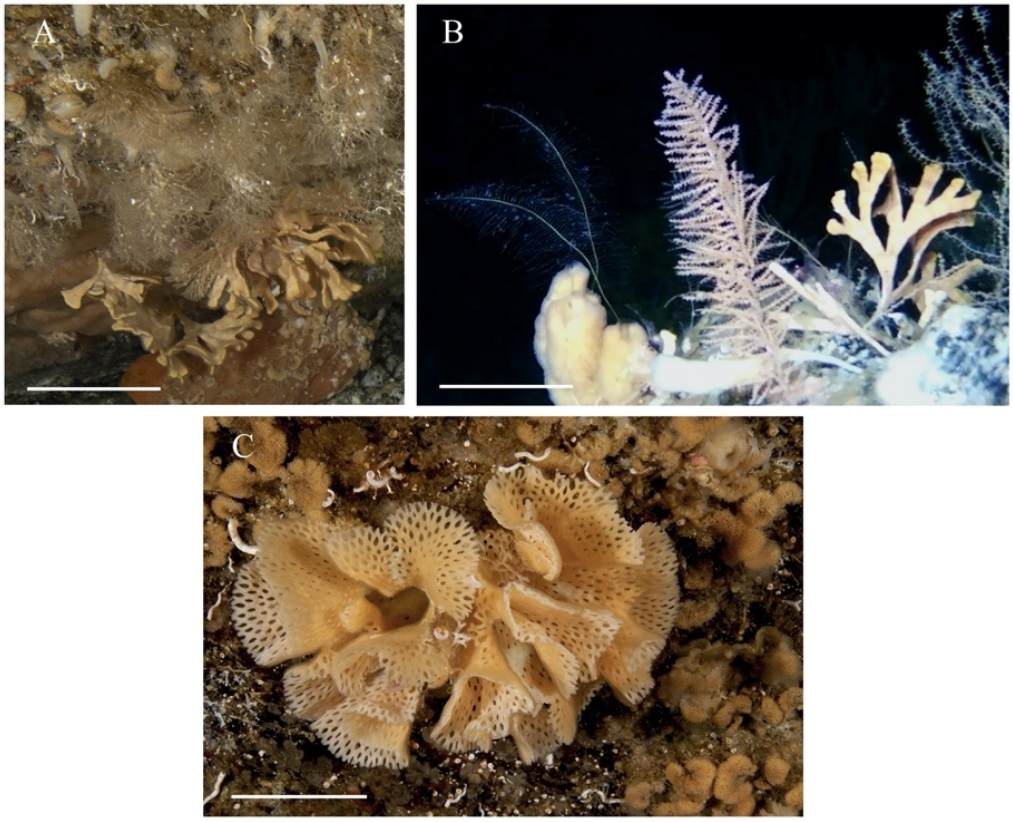

Figure 2. Bryozoan colonies in their natural habitat (**A**) *Cellarinella* sp.1 living at 25 m depth; (**B**) *Cellarinella* sp.2 (right) living at 110 m depth; (**C**) *Reteporella* sp. living at 25 m depth. Scale bars: 3 cm. Pictures: A, C: P. Kuklinski; B: E. Spirandelli.

2.2. Morphological and Skeletal Investigations

After sampling, the three species were photographed with the aim of illustrating the branch morphology of freshly collected colonies before cleaning. Images were taken with a Digital Nikon D750 Camera (Nikon, Tokyo, Japan), equipped with AF-S VR Micro-Nikkor 105 mm f/2.8G IF-ED objective.

For taxonomical identification *via* analyses of the morphological features [59,60], some of the specimens were carefully cleaned to remove the organic components (i.e., cuticle and polypides). In order to remove the organic material, samples were soaked for 5 days in a solution of 20 % sodium hypochlorite, checked daily for changes in organic state of removal, then washed thoroughly in tab water and dried. Taxonomic identification was aided by imaging using a CamScan MX 2500S (CamScan Electron Optics, Finchley, London, United Kingdom) scanning electron microscope (SEM) with a LaB6 cathode, equipped with a system for backscattered electrons imaging (BEI) and an EDAX Sapphire Si (Li) energy-dispersive X-ray detector (EDAX, Inc., Pleasanton, CA, USA). SEM-EDS investigations (operating conditions: ca. 20 kV accelerating voltage and 160 nA beam current) were performed on carbon-coated freshly broken samples.

In order to identify and analyze growth check lines, three-dimensional models of the three species were obtained using a bench-top Skyscan 1172 micro-CT system (Bruker), equipped with a Hamamatsu 100/250 microfocus X-ray source and a Hamamatsu C9300 11-megapixel camera (camera pixel size = 9.0 μm) filtered by a 0.5 mm aluminum foil. Images were acquired in step and shoot motion type with round scanning trajectory (0.22° scan

rotation step over 360°) and 1000 ms exposure time under the following working conditions: source voltage = 100 kV, current = 100 µA. In order to minimize noise, each image derived from an average of 10 frames obtained in 2 × 2 camera binning mode with a vertical random movement of 10 µm. Because of the sample height, four *Cellarinella* sp.1 and *C*. sp.2 and five *Reteporella* sp. connected scans were used and the total run time for each specimen was between 16 and 20 h. From raw images projection, stacks of ~ 4000 to 5100 images (image size: 2000 × 2000 pixels, pixel size ~ 6 µm) were reconstructed, applying thermal correction, misalignment compensation, ring artefact reduction and beam hardening correction using the NRecon® (Bruker) software package. Segmentation within a pre-selected ROI was performed with CT Analyzer® (Bruker) software package by using a 3D-adaptive thresholding procedure (mean of minimum and maximum value within spherical kernels of eight pixels' radius) starting from a pre-determined pre-thresholding value, and a despeckle routine in the 3D space. Resulting images were saved as monochrome bitmaps (1 bit) and then transformed into 3D-renders and animations with CTVox® software package (Bruker).

Zooid morphometrics (zooid length, primary orifice length and width of approx. 20 complete and adult zooids per band) were measured from scanning electron micrographs, whereas the high-quality micro-CT scans obtained for each species were used to measure growth check line thickness, and basal, lateral and frontal zooidal wall thickness (30 replicated measurements per growth band). Image Software (ImageJ 1.53r) was used for morphological measurements that were conducted on adult and non-reproductive zooids.

2.3. Biomineralization—The Skeletal Organic Matrix

2.3.1. Cleaning and Extraction

A sample of 3–5 branches of each bryozoan species were delicately cleaned with a toothbrush to remove the epibionts, then soaked overnight in 10× diluted sodium hypochlorite (0.6%–1.4% active chlorine) solution, under constant stirring. After this first bleaching step, the branches were rinsed with milli-Q water in an ultrasonic bath (ultrasonic cleaner Branson 200, Soest, The Netherlands) for 15 min. Finally, they were soaked in ethanol and dried in an oven (Firlabo BC120, Emerainville, France) at 37 °C. This allowed the removal of animal tissues, as well as other associated organisms. To complete the cleaning, the bryozoan skeletons were crushed into ∼2 mm fragments manually in an agate mortar and the fragments were immersed in sodium hypochlorite (0.6%–1.4% active chlorine) and left gently turning overnight (second bleaching). The bleached fragments were successively washed with double-distilled water, dried, and powdered by using a mortar grinder (Fritsch Pulverisette 2, Idar-Oberstein, Germany). The powders were sieved (pore size < 200 µm), bleached overnight in NaClO solution (third bleaching), thoroughly washed and air-dried at 37 °C before decalcification.

For each species, the cleaned powders (from 1.36 g to 9.05 g) were suspended in cold water and decalcified overnight at 4 °C by progressively adding 200 µL every 10 s cold dilute acetic acid (10%) with a Titronic Universal electronic burette (Schott Instruments, Mainz, Germany). After decalcification, the clear solutions (from 60 to 450 mL) were centrifuged (3900 G, 30 min) in order to separate the pellet containing the acid-insoluble matrix (i.e., AIM) from the supernatant (i.e., the acid-soluble matrix–ASM). The AIM pellets were resuspended in Milli-Q water, centrifuged, and the supernatant discarded. After three rinsing cycles, the AIM pellets were lyophilized in a Cryodos freeze-dryer (Telstar, Terrassa, Spain).

The ASM solutions were concentrated by ultrafiltration (Aicon stirred cell 400 mL) on a 3 kDa cut-off membrane (Millipore). The retentates (15 mL or less) were collected while the permeates (the fraction that passed through the 3 KDa membrane) were stored frozen. All concentrated ASM retentates (>3 kDa) were extensively dialyzed for 2 days against 1 L MilliQ water in Spectra/Por® 6 dialysis tubing (pre-wetting RC tubing, cut-off 1 kDa) with 5–6 water changes, before being lyophilized. All lyophilized fractions were carefully weighed on an analytical precision balance (Quintix35-1S model, Sartorius, Göttingen, Germany).

2.3.2. SDS-PAGE

The skeletal extracts were analyzed by SDS-PAGE (Mini Protean III gels, Bio-Rad, Hercules, CA, USA), on precast gradient gels (Mini-PROTEAN TGX Gel 4%–20% acrylamide, 90 mm × 70 mm, BioRad) or on 12% acrylamide hand-cast gels. Before the electrophoresis, samples (*Cellarinella* sp.1, *Cellarinella* sp.2, *Reteporella* sp., and *Cellarinella* sp.1—PRE (pre-bleached)) were treated as follows: ASM lyophilizates were suspended in Milli-Q and an aliquot was added to an equal volume of 2× Laemmli sample buffer containing β-mercaptoethanol. AIM pellets were fragmented with a scalpel and a part was directly resuspended in 1× Laemmli sample buffer. All extracts were heat-denatured (5 min, 99 °C) before being cooled on ice and briefly centrifuged. The solubilized fractions of the AIMs (supernatants), referred to as LS-AIMs (Laemmli-Soluble-Acid-Insoluble Matrix) and the ASMs were analyzed on gel. For *C. nutti*—pre (pre-bleached), only the ASM (pre-ASM) was analyzed on gels. After migration, the gel was stained with silver nitrate, according to the Morrissey protocol [61] with few modifications [62]. The experiment was repeated three times.

2.3.3. Fourier Transform—Infra Red Spectroscopy (FT-IR)

FT-IR spectroscopy was used to check the calcium carbonate polymorphs of the cleaned powders and the overall chemical properties of the extracted AIMs of the three species, after two or three bleaching steps. Minute chips of lyophilized samples were analyzed with a Bruker Vector 22 instrument (Bruker Optics Sarl, Marne la Vallée, France) fitted with a Specac Golden Gate Attenuated Total reflectance (ATR) device (Specac Ltd., Orpington, UK) in the 4000–500 cm^{-1} wavenumber range (twelve scans at a spectral resolution of 4 cm^{-1}). The choice for ATR mode was driven by its reliability and reproducibility [63]. The qualitative assignment of absorption bands was performed manually by comparing previously described spectra, available in-house catalogue or from the literature [64,65].

2.3.4. Enzyme-Linked Lectin Assay (ELLA)

To obtain a qualitative sugar signature of ASM extracts, ELLA (Enzyme Linked Lectin Assay) tests were performed on the three species according to Kanold and coauthors' protocol [65,66]. Due to the high insolubility of AIM and the reduced ability of LS-AIM to bind the microplate polymer, these two fractions were not tested. The three bryozoan ASMs were incubated (50 ng/well) in 96-well plates (MaxiSorp, Nunc/Thermo Scientific, Nunc A/S, Denmark) for 90 min at 37 °C. They were subsequently washed three times with a TBS/Tween-20 solution (0.5 mL Tween 20 per L) owing to a manual microplate 8-channel washer (Nunc Immuno Wash, Denmark), then blocked with Carbo-free blocking solution (Vector Laboratories, UK) for at least 30 min at 37 °C. The plates were incubated 90 min. at 37 °C with 21 biotinylated lectins (Vector Laboratories, UK, kit I, II and III) diluted 100 (kit III) or 200 times (kits I & II) in TBS/Tween-20/Carbo-free solution. The test was performed with quadruplicates of each lectin. Plates were washed three times with TBS/Tween-20 to remove the unbound lectins, before being incubated with a solution of alkaline phosphatase-conjugated avidin (1:70,000 in TBS, Avidin-AP, Sigma, A7294, St. Louis, MO, USA) for 90 min at 37 °C. The microplates were washed five times, and incubated with the substrate buffer solution (10% vol/vol diethanolamine in Milli-Q water, pH 9.8) containing phosphatase substrate (0.5 mg/mL, 4-nitrophenyl phosphate disodium salt hexahydrate (pNPP) tablet, Sigma, USA) at 37 °C. The plate was incubated at 37 °C and successive optical readings were performed every 15 min at 405 nm with a microplate spectrophotometer (Bio-Rad 680 microplate reader, Hercules, CA, USA). The results (Table 1) were normalized and translated in percentage of reactivity by subtracting the background and considering the highest response as 100%. For each extract, the test was repeated three times.

Table 1. Biotinylated Lectins: code (1, 2, 3 series), abbreviation, extract name and type. Binding preference and specificities of each lectin are reported in 65 and 66.

Code	Abbreviation	Extract Name	Lectin Type
A1	Con A	*Canavalia ensiformis*	D-Mannose/D-Glucose/N-acetylglucosamine
B1	SBA	*Glycine max*	Galactose/N-acetylgalactosamine
C1	WGA	*Triticum vulgare*	Chitin-binding lectins/N-acetylglucosamine/N-acetyllactosamine
D1	DBA	*Dolichos biflorus*	N-acetylgalactosamine
E1	UEA I	*Ulex europaeus*	Fucose
F1	RCA 120	*Ricinus communis*	Galactose/N-acetylgalactosamine
G1	PNA	*Arachis hypogaea*	Galactose/N-acetylgalactosamine
A2	GLS I	*Griffonia simplicifolia*	Galactose/N-acetylgalactosamine
B2	PSA	*Pisum sativum*	D-Mannose/D-Glucose/N-acetylglucosamine
C2	LCA	*Lens culinaris*	D-Mannose/D-Glucose/N-acetylglucosamine
D2	PHA-E	*Phaseolus vulgaris*	Galactose/N-acetylglucosamine/Mannose
E2	PHA-L	*Phaseolus vulgaris*	Galactose/N-acetylglucosamine/Mannose
F2	SJA	*Sophora japonica*	Galactose/N-acetylgalactosamine
G2	Succinylated WGA	*Triticum vulgare*	Chitin-binding lectins/N-acetylglucosamine/N-acetyllactosamine
A3	GLS II	*Griffonia simplicifolia*	N-acetylglucosamine
B3	DLS	*Datura stramonium*	Chitin-binding lectins/N-acetylglucosamine/N-acetyllactosamine
C3	ECL	*Erythrina cristagalli*	N-acetyllactosamine/N-acetylgalactosamine
D3	Jacalin	*Artocarpus integrifolia*	Galactose/N-acetylgalactosamine
E3	LEL	*Lycopersicon esculentum*	Chitin-binding lectins/N-acetylglucosamine/N-acetyllactosamine
F3	STL	*Solanum tuberosum*	Chitin-binding lectins/N-acetylglucosamine/N-acetyllactosamine
G3	VVA	*Vicia villosa*	N-acetylgalactosamine

2.4. Seawater Isotopic Composition and DIC at Sampling Site

2.4.1. Sea-Water Isotopy of $\delta^{18}O$ and $\delta^{2}H$

Isotope ratio infrared spectroscopy (IRIS) was used to measure a seawater sample (4 replicates) taken from 25 m depth at Site 1 in November 2018, to obtain the local $\delta^{18}O$ and $\delta^{2}H$ composition. Analyzes were carried out with an L 1102-i WS-CRDS Picarro analyzer (Picarro Inc., Santa Clara, CA, USA), based on wavelength-scanned cavity ring-down spectroscopy. Values are reported vs. Vienna standard mean ocean water (VSMOW) in the standard δ-notation in permille (‰):

$$\delta = (R_{\text{sample}}/R_{\text{reference}} - 1) \quad (1)$$

where R is the ratio of the numbers (n) of the heavy and light isotope of an element (e.g., $n(^{18}O)/n(^{16}O)$) in the sample and the reference material [67].

The sample was measured on four sequential injections and raw data were corrected for sample-to-sample memory; the reported value is the mean value. Data sets were corrected for instrumental drift during the run and normalized to the VSMOW/SLAP (standard light Antarctic precipitation) scale by assigning a value of 0‰ and −55.5‰ ($\delta^{18}O$)/0‰ and −427.5‰ ($\delta^{2}H$) to VSMOW2 and SLAP2, respectively [68]. For normalization, two laboratory reference materials, calibrated directly against VSMOW2 and SLAP2, were measured in each run. External reproducibility, based on repeated analyses of a control sample, was better than 0.1 ‰ and 1 ‰ (±1 sigma) for $\delta^{18}O$ and $\delta^{2}H$, respectively. For details of the described procedures refer to [69].

2.4.2. Carbon Stable Isotope ($\delta^{13}C_{DIC}$) in Seawater—Gasbench-IRMS

The water sample was analyzed for $\delta^{13}C_{DIC}$ (DIC—dissolved inorganic carbon) by an automated equilibration unit (Gasbench 2; Thermo Fisher Scientific, Bremen, Germany) coupled in continuous flow mode to a Delta *plus* XP isotope ratio mass spectrometer (Thermo Fisher Scientific, Bremen, Germany). Four replicates were extracted from the 1.5 L sample bottle with 1 mL disposable syringes, and the removed volume was simultaneously replaced by inert argon gas. The replicates were injected into 12 mL Labco Exetainers™ (Labco Ltd. Lampeter, UK) that were prepared with phosphoric acid and pre-flushed with helium (purity 99.999%). The sample weight was adjusted to attain a

detector signal height between ~6.0 and ~7.5 V (m/z 44) for the isotope ratio mass spectrometer [70,71]. Values are reported in the standard δ-notation in per mil (‰) vs. Vienna Pee Dee Belemnite (VPDB), as in Equation (1), where R is the ratio of the numbers (n) of the heavy and light isotope of an element (e.g., $n(^{13}C)/n(^{12}C)$). Data were corrected for instrumental drift and normalized to the VPDB scale by assigning a value of +1.95 ‰ and −46.6 ‰ to NBS 19 and LSVEC, respectively [68]. External reproducibility was based on the repeated analyses of a control sample prepared from sodium bicarbonate and DIC-free, ultrapure water (Milli-Q Integral, EMD Millipore Corporation, Billerica, MA, USA). Precision of the control sample was better than 0.1 ‰ (1 sigma) for $\delta^{13}C_{DIC}$.

2.4.3. DIC Concentration—Gasbench-IRMS

Concentration of total dissolved inorganic carbon (DIC) was determined from the peak areas of the chromatogram of the isotope ratio measurement. The sample peak areas were directly proportional to the amount of CO_2 liberated from the reaction with phosphoric acid. A set of standards with known DIC concentrations was prepared by dissolving $NaHCO_3$ in DIC free water and included in every run. The peak areas were adjusted for the exact individual sample volume. The exact amount of water in each vial was determined by weighing. For the conversion to the volume, a sample density of 1.025 g cm^{-3} for seawater and 1000 g cm^{-3} for freshwater were assumed. DIC concentration was reported in milli mol per liter (mmol L^{-1}). The analyses' accuracy was monitored by repeated analysis of the standard. Precision (i.e., reproducibility) was better than 5% relative standard deviation (RSD). Conversion factor to mg L^{-1} (=ppm C) is 12.011 (carbon atomic weight); e.g., 1.0 ppm C = 0.0833 mmol L^{-1}.

3. Results

3.1. Morphological Identification and Skeletal Structures

3.1.1. Species Identity

Morphological investigations revealed two different *Cellarinella* species, *C. nutti* Rogick 1965 and *C. njegovanae* Rogick 1956, collected at 25 m and at 110 m, respectively. Specimens belonging to the genus *Reteporella* were identified as *Reteporella frigida* Waters 1904.

A *Cellarinella nutti* colony, collected at 25 m of depth at Site 1, showed dichotomous branches and was anchored to rocky boulders using flexible rhizoids (Figure 2A). The colony, exceeding 100 mm in height, was pale orange in color when alive and turned brownish after death (Figure 3A). *C. nutti* branches were characterized by 6–7 growth check lines and about 30 longitudinal series of autozooids on each side of the branches of the bilaminar colony. Analyses of zooid morphometric traits, conducted on each band, revealed autozooid lengths ranging from 62 up to 1190 µm, becoming uniformly reticulated due to secondary calcification processes occurring in later ontogeny (Figure 4A). Zooid length varied from the proximal to the distal part of the growth band (gb), but, also, differences were found among the bands (Table S1). Shorter zooids were generally found in the proximal part of the growth band, whereas the longest were in the middle part (Table S1). The primary orifice—generally wider than long (length: 160–290 µm, width: 240–380 µm)—showed an overhanging distal edge and a smooth, flat oral shelf, extended distolaterally from the proximal edge. The zooids were approximately 1.0 × 0.5 mm in size. Brood chambers (i.e., ovicells) were present in almost all bands between growth checks, generally in the middle of the bands, and were spherical, smooth, and well calcified, sometimes immersed in later ontogeny (Figure 4B). The primary orifice—broader than long—showed a distal rim with smooth, projecting hood, whereas the proximal rim was occupied by a transversely oriented avicularium. In many zooids, a secondary avicularium (i.e., defensive structure) bearing a triangular mandible was found proximolaterally to the orifice (Figure 4C). The avicularium apex occupied a short, thick, umbonate process, which was often followed by a secondary process developing proximal to the aperture and close to the proximal part of the avicularium.

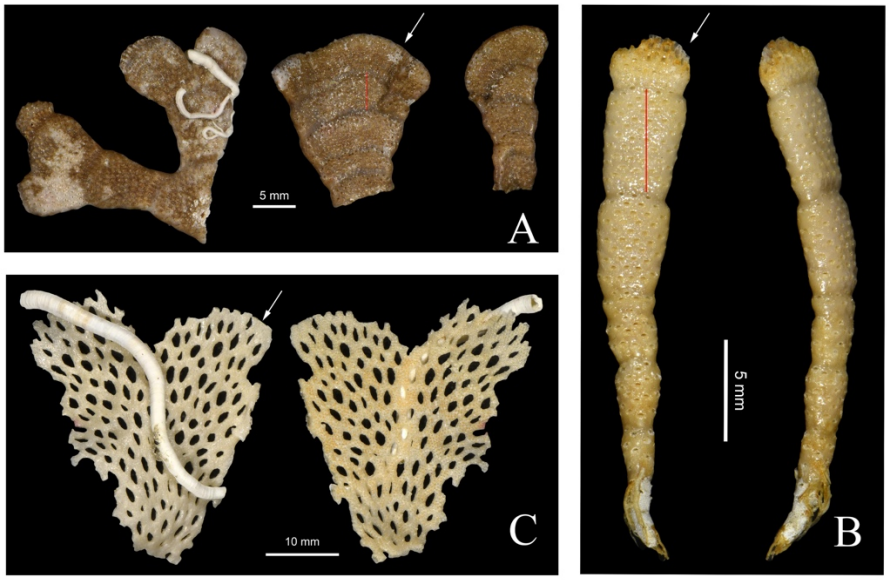

Figure 3. Images of live study material: (**A**) *Cellarinella nutti*; (**B**) *Cellarinella njegovanae*; (**C**) *Reteporella frigida*. Arrows show the growing edges (distal part of the colony). Red lines show the annual growth band between two growth checks.

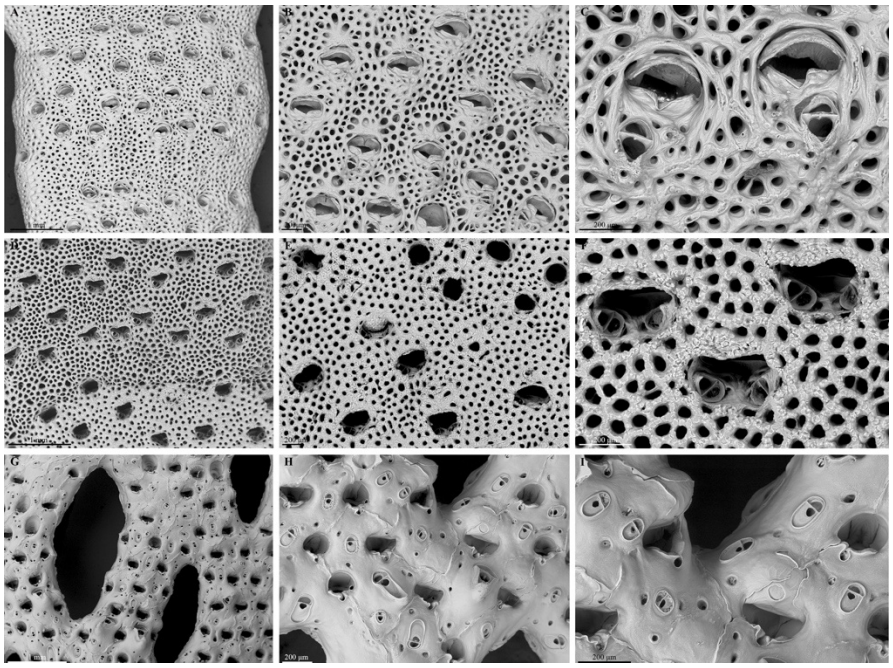

Figure 4. Scanning electron micrographs (SEM images) of the target species. (**A**–**C**) *Cellarinella nutti*: (**A**) portion of the branch including one year of growth; (**B**) detail of zooids and immersed ovicells (i.e., brooding chambers); and (**C**) close- up of feeding autozooids with avicularia. (**D**–**F**) *Cellarinella njegovanae*: (**D**) portion of the branch between two annual growth bands; zooid boundaries obscured by secondary calcification; (**E**) detail of zooids with hypercalcified frontal walls; ovicells completely immersed; and (**F**) feeding autozooids with paired avicularia lodged in the proximal corners of the primary orifice. (**G**–**I**) *Reteporella frigida*: (**G**) portion of the colony showing the fenestrules; (**H**) detail of zooids with regular avicularia on the frontal walls and large avicularia with triangular rostra, sharply hocked; and (**I**) feeding and ovicellate zooids with avicularia. Scale bars: 1 mm, 200 μm.

Cellarinella njegovanae, collected at 110 m in Site 2, was an important component of bioconstructional ecosystems of the bay below 100 m depth, together with sponges

and corals. On soft bottoms, branching colonies often exceeding 60 mm in height were found on rocky boulders or colonizing other erect forming species. Bilaminar branches of *C. njegovanae*, bright yellow when alive and thinner than those of *C. nutti* (rarely exceeding 8 mm of width), employed chitinous rhizoids for anchoring to the substrate. The collected specimens displayed five to eight growth check lines per branch. The analyses of zooidal morphometric traits revealed that, in each band, autozooids were arranged in five to twelve alternating longitudinal series, with indistinct lateral boundaries (Figures 1B, 3B and 4D). Autozooid length ranged from 680 up to 1160 µm, with longest zooids at the proximal part of each band (Table S1). The primary orifice—generally wider than long (length: 160–290 µm, width: 290–360 µm)—showed an overhanging distal edge and a smooth, flat oral shelf, extending distolaterally from the proximal edge. The widest primary orifices were found in zooids in the middle parts of the branches (Table S1). Ovicells were hardly detectable because they are deeply immersed, especially in the proximal part (Figure 4E). Avicularia were paired, each one located at the proximal corner of the primary orifice. The acute rostrum, bearing a short triangular mandible, was directed distolaterally (Figure 4F).

Reteporella frigida colonies formed complex three-dimensional bioconstructions with folded, reticulated sheets, (Figures 1C and 3C) at Site 1. Pale pink, colonies were able to exceed 150 mm in height and expand laterally by creating lightly calcified and brittle voluminous colonies. The ramifying branches which anastomosed to form the holes called fenestrules, normally consisted of eight zooid series (Figure 4G) and lacked growth check lines. Autozooids were convex (length: 740–980 µm, width: 290–400 µm), clearly defined at the growing edge but with sutures, which were hardly distinguishable across the colony. Zooidal frontal walls were smoothly calcified, with two or three marginal pores. The primary orifice was wider than long (length: 140–190 µm, width: 170–220 µm), with the distal edge finely denticulate and possessing condyles, becoming deeply immersed in early ontogeny. The peristome developed proximally as a folded, reflected lip, with a rounded, eccentrically placed notch. The specimen had spines which protruded on each side. Avicularia were extremely abundant, located on zooidal frontal walls, most frequently oval, proximally directed and with a crossbar and an extensive palate (Figure 4H). Large avicularia generally occurred within each fenestrule, proximal to the peristome and also had a triangular rostrum, sharply hooked at its tip and projecting at an acute angle to frontal plane of the colony. Brood chambers, as wide as long, were flattened frontally with a short, rounded median fissure. Relatively conspicuous in the youngest parts of the colony, these ovicells became deeply immersed in the oldest parts of the branches (Figure 4I).

3.1.2. Skeletal Characteristics

MicroCT revealed changes in skeletal wall thickness within the six growth bands (gb) characterizing *Cellarinella nutti* branches (Figure 5). From proximal (i.e., recently formed, band n 1, probably year: 2017) to distal part of the branch (i.e., the oldest branch, probably year 2012), a progressive increase in growth band length was observed (max gb1: 4099 µm, min gb6: 1449 µm) (Table 2). Longitudinal and transverse sections of the branch showed a progressive thickening of both lateral and basal zooidal walls in correspondence to the growth check lines (Figure 5) (gcl). Measurements were conducted on zooid basal and frontal walls (n = 30) in the growth band and in correspondence of growth check lines. Across gb, a decrease in zooidal wall thickness from the proximal (oldest) to the distal (youngest) edge was observed (basal wall: gb1= 45.9 $\pm$ 6.8 µm, gb6= 26.6 $\pm$ 5.6 µm; lateral wall: gb1= 51.6 $\pm$ 9.0 µm gb6= 30.8 $\pm$ 9.3 µm). When reaching gcl, zooids showed skeletal walls two times (lateral walls) and three times (basal walls) thicker than those of autozooids from other parts of the gb. In detail, the ratios between zooid basal wall thickness in the gcl compared with the basal gb (i.e., RbwT gcl/gb) (Table 3) ranged from 3.0 to 4.9, with the smallest value in gb1 (distal) and the largest value in gb6 (proximal), respectively. Lateral wall ratios (i.e., RlwT gcl/gb) ranged from 2.2 to 3.5, with the smallest ratio found in gb1 and the largest ratio in gb5 (Table 3 and Figure 5).

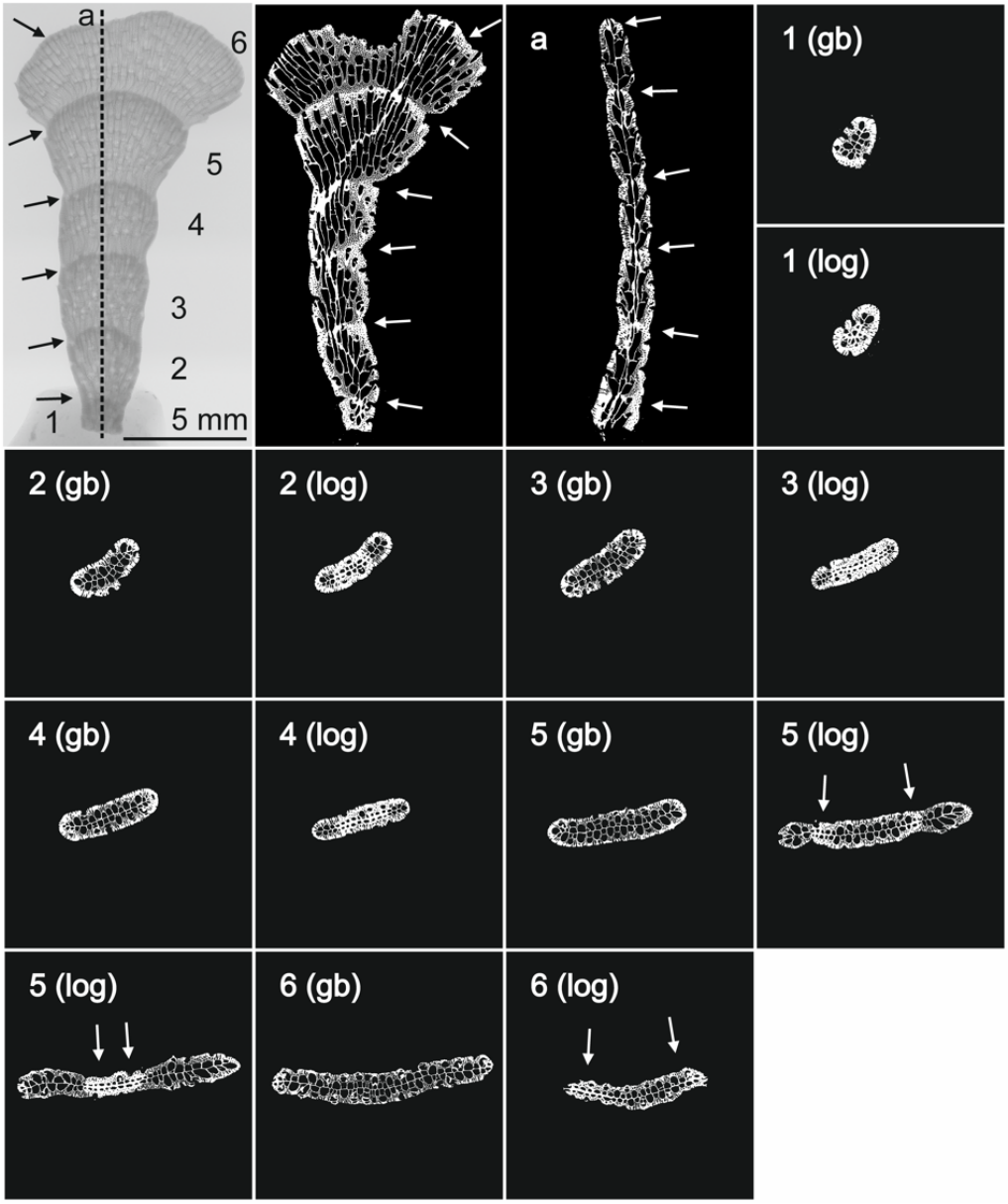

Figure 5. Micro CT images of *Cellarinella nutti*. Radiographic image of the whole branch (scale bar: 5 mm) showing the growth bands (arrowed) (**1**–**6**) and the branch axis (**a**). Frontal and lateral longitudinal sections of the whole branch; 13 transverse sections of the growth bands (gb) (**1**–**6**) and growth check lines (gcl) (**1**–**6**). Scale bar for micro CT images: 5 mm.

Cellarinella njegovanae branches, collected from different colonies, were characterized by having approx. five growth bands (Figure 6). Differently from *C. nutti*, variability in gb length was observed across *C. njegovanae* branches, with a minimum length of 1974 µm for gb3 and maximum of 7127 µm for gb2 (distal and old part of the branch) (Table 2). Similarly to *C. nutti*, longitudinal and transverse sections of the branches showed a progressive thickening of both lateral and basal zooidal walls corresponding to the locations of the gcl (Figure 6). Repeated measurements (n = 30) conducted on zooid basal and frontal walls across the gb and at the gcl showed a decreasing trend in zooidal wall thickness, from the proximal (oldest) to the distal (youngest) edge, with some variability. Specifically, for basal walls: gb1 = 56.7 ± 13.5 µm, gb6 = 25.7 ± 7.5 µm; for lateral walls: gb1 = 49.1 ± 16.4 µm gb5 = 26.8 ± 6.3 µm). When reaching a gcl, *C. nutti* zooids showed skeletal walls, both basal and lateral, approx. two times thicker than those from other parts of the gb. The ratios

RbwT gcl/gb (Table 3) ranged from 2.3 to 5.9, with the smallest value in gb3 and the largest value in gb5 (proximal), respectively. Lateral wall ratios (i.e., RlwT gcl/gb) ranged from 2.9 to 5.4, with the smallest ratio found in gb1 and the largest ratio in gb5 (Table 3, Figure 6).

Reteporella frigida did not form any growth check lines on either side of the colony (Figure 7). Longitudinal and transverse sections conducted with the micro-CT allowed measurement of basal wall thickness (166.9 ± 40 µm), lateral wall thickness (31.9 ± 9.1 µm) and frontal wall thickness (226.0 ± 33.5 µm) (Table 3) of adult autozooids.

Table 2. Growth band number (n gb) and length (gbL) (µm) in *Cellarinella nutti* and *Cellarinella njegovanae* branches. Mean number of growth bands (n band) are reported per colony per species in a decreasing order, from the youngest (n 6) just below the growing edge, to the oldest part of the branch (n 1).

Species	n gb	gbL (µm)
Cellarinella nutti	6	1449
	5	3360
	4	3547
	3	3286
	2	4274
	1	4099
Cellarinella njegovanae		
	6	3685
	5	7127
	4	1974
	3	3384
	2	5859
	1	2829

Table 3. Number of growth bands (n gb), zooid basal wall thickness from growth bands (bwT_{gb}) (µm), zooid basal wall thickness at growth check lines (bwT_{gcl}) (µm), ratio between bwT_{gcl} bwT_{gb} (RbwT gcl/gb); zooid lateral wall thickness from growth bands (lwT_{gb}) (µm), zooid lateral wall thickess at growth check lines (lwT_{gcl}) (µm) and ratio between lwT_{gcl} lwT_{gb} (RlwT gcl/gb); frontal wall thickness (fwT) in *Cellarinella nutti* and *Cellarinella njegovanae*. BwT, lwT and fwT in *Reteporella frigida*. Averages (n = 30) ± s.d.

Species	n°gb	bwT_{gb} (µm)	bwT_{gcl} (µm)	RbwT gcl/gb	lwT_{gb} (µm)	lwT_{gcl} (µm)	RlwT gcl/gb	fwT (µm)
Cellarinella nutti	6	45.9 ± 6.8	140.0 ± 24.0	3.0	51.6 ± 9.0	115.1 ± 20.3	2.2	316.6 ± 86.3
	5	33.7 ± 6.8	125.1 ± 6.8	3.7	33.4 ± 9.0	94.2 ± 9.0	2.8	
	4	33.0 ± 7.5	135.8 ± 21.1	4.1	31.6 ± 7.2	101.2 ± 17.4	3.2	
	3	30.6 ± 4.5	118.0 ± 20.3	3.9	36.3 ± 7.7	106.5 ± 16.8	2.9	
	2	32.5 ± 4.3	119.9 ± 19.3	3.7	31.1 ± 7.2	108.5 ± 19.8	3.5	
	1	26.6 ± 5.6	130.4 ± 18.9	4.9	30.8 ± 9.3	105.7 ± 13.3	3.4	
Cellarinella njegovanae	6	56.7 ± 13.5	184.7 ± 23.8	3.3	49.1 ± 16.4	142.0 ± 15.7	2.9	445.0 ± 80.3
	5	42.4 ± 13.5	171.0 ± 13.5	4.0	41.7 ± 16.4	142.8 ± 16.4	3.4	
	4	51.6 ± 9.1	118.5 ± 20.1	2.3	46.3 ± 11.5	181.1 ± 34.4	3.9	
	3	37.9 ± 9.8	165.5 ± 30.5	4.4	37.4 ± 8.6	143.6 ± 27.9	3.8	
	2	29.6 ± 7.2	173.2 ± 28.6	5.9	26.8 ± 6.3	146.3 ± 31.3	5.4	
	1	25.7 ± 7.5			29.2 ± 6.9			
Reteporella frigida		166.9 ± 40			31.9 ± 9.1			226.0 ± 33.5

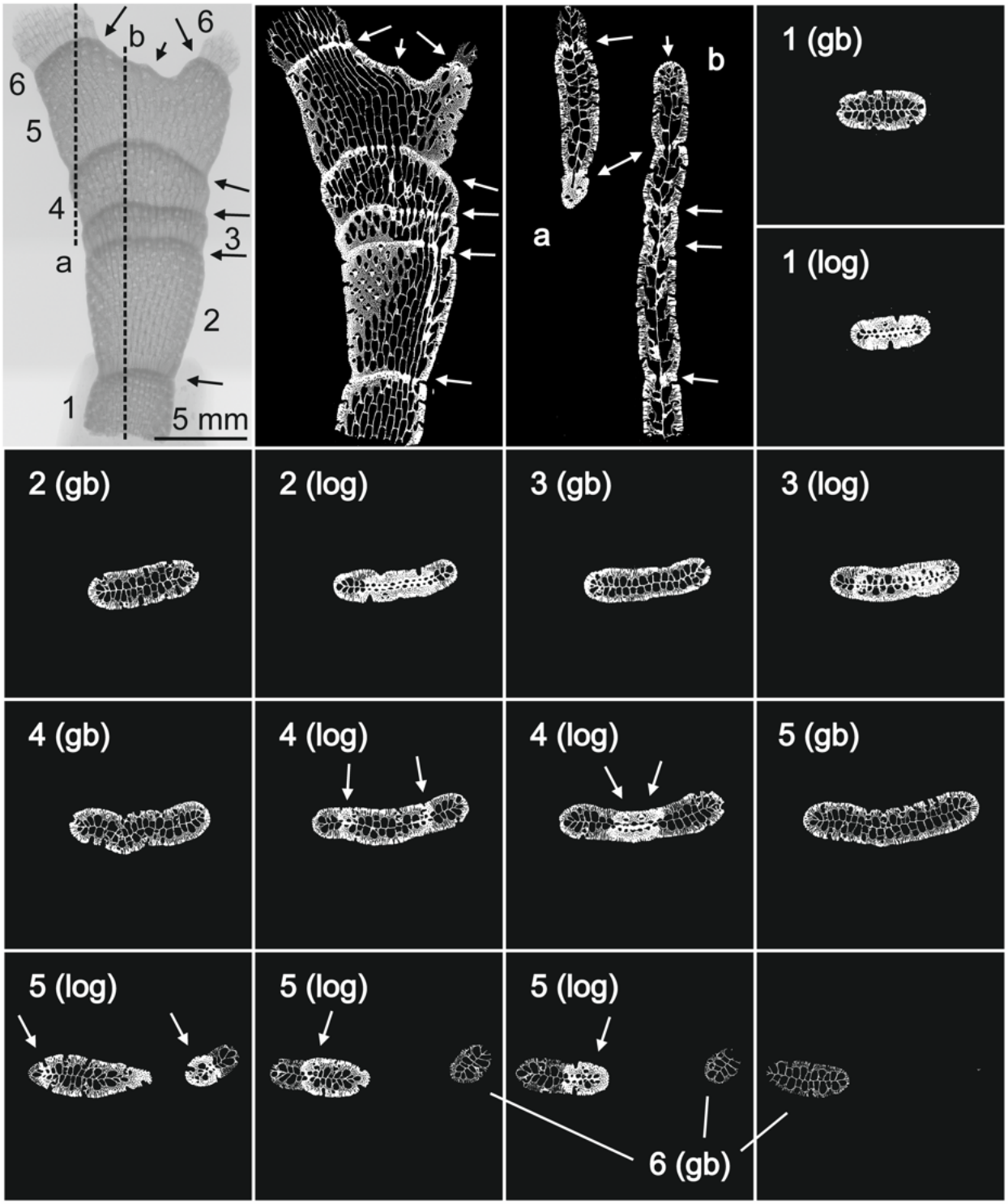

Figure 6. Micro CT images of *Cellarinella njegovanae*. Radiographic image of the whole branch (scale bar: 5 mm) showing the growth bands (**1**–**5**) (arrowed) and two branch axes (**a**,**b**) for longitudinal sections. Band 6 corresponds to the growing edge. Frontal and lateral (**a**,**b**) longitudinal sections of the whole branch; 14 transverse sections corresponding to the growth bands (gb) (**1**–**5**)and growth check lines (gcl) (arrowed) (**1**–**5**). Scale bar micro CT images: 5 mm.

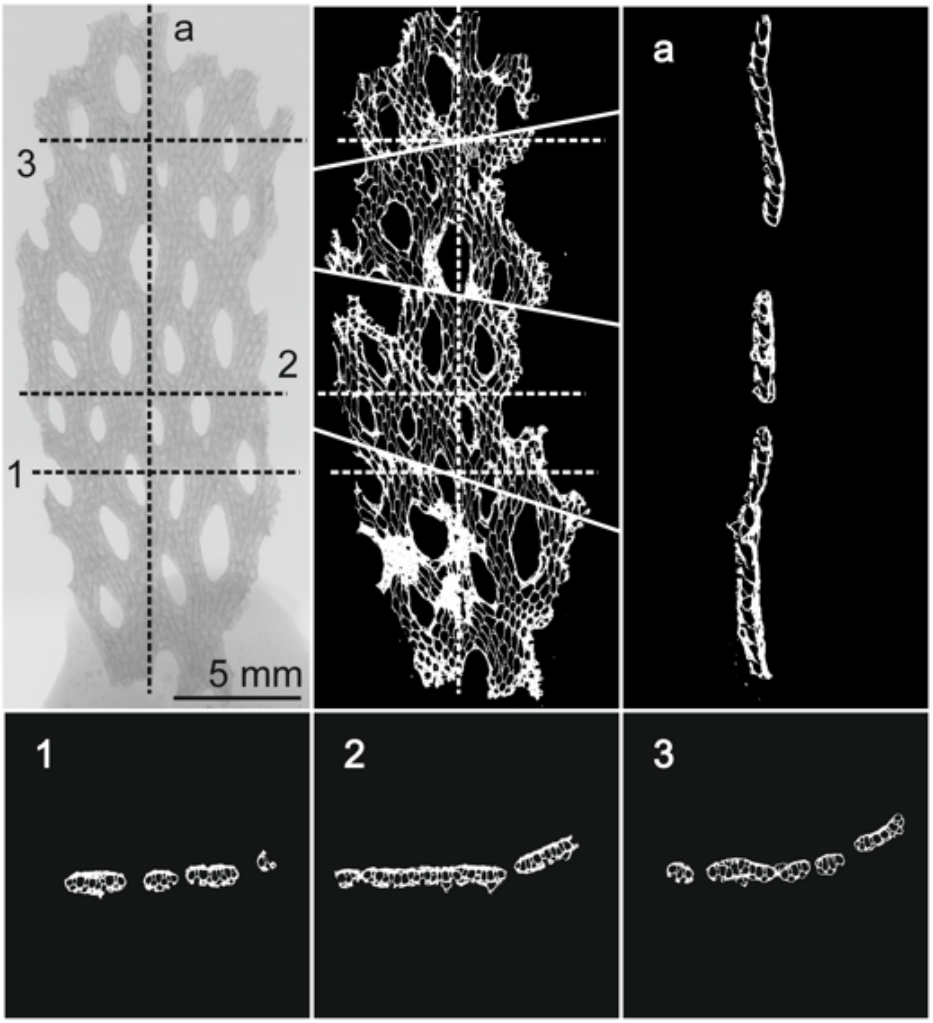

Figure 7. Micro CT images of *Reteporella frigida*. Radiographic image of the whole colony fragment (scale bar: 5 mm) showing the longitudinal axis (**a**) and three transverse sections (**1**–**3**). Scale bar micro CT images: 5 mm.

3.2. Biomineralization—The Skeletal Organic Matrix

3.2.1. Quantification of the Matrix and SDS PAGE

The quantification of the matrix extracted from *Cellarinella nutti*, *C. nutti* PRE (pre-bleached), *Cellarinella njegovanae* and *Reteporella frigida* are shown in Table 4. All ASM fractions represented less than 0.05 % of the skeletal weight, while AIMs ranged from 0.04 to >0.7%. The total skeletal matrix (ASM + AIM) ranged from 0.1% of the skeletal powder (*C. nutti*) to almost 0.75% (*C. njegovanae*). Surprisingly, the ASM/AIM ratios were very different between the extracts. While this ratio ranged from 0.3 to 1.2 in *C. nutti* and *C. nutti* PRE, respectively, it fell to 0.06 for *C. njegovanae* and 0.02 for *R. frigida*, indicating that these two skeletal matrices were mostly insoluble in acetic acid.

The ASM and the LS-AIM were analyzed by polyacrylamide gel electrophoresis (SDS-PAGE) after staining with silver nitrate; the results are shown on Figure 8. All matrices (ASM and LS-AIM) were characterized by smearing non-discrete molecules, a property often observed in matrices associated with calcium carbonate biominerals. In addition, *C. nutti* ASM was characterized by one strong discrete band around 55 KDa and at least eight more diffuse bands between 55 and 20 kDa. The pattern of *C. nutti* LS-AIM exhibited similarities with that of the ASM. The pattern of both *C. njegovanae* extracts were rather similar, with one thick band around 20–22 kDa and a few diffuse bands of higher molecular weight. The matrices of *R. frigida* were extremely tenuous, suggesting either that they were

poorly concentrated (in spite of having been loaded in similar concentrations as the other samples) or that they did not stain well with silver.

Table 4. Quantification of powder weight (g), ASM and AIM, total matrix (% weight ± s.d.) and ASM/AIM extracted from *Cellarinella nutti*, *C. nutti* PRE, *Cellarinella njegovanae* and *Reteporella frigida* skeletons. ASM: Acid-soluble matrix. AIM: Acid-insoluble matrix. PRE = pre-bleached.

Sample	Powder Weight gr	ASM mg (% Weight)	AIM mg (% Weight)	Total Matrix mg (% Weight)	ASM/AIM Ratio
C. nutti	9.05	2.24 ± 0.024	7.25 ± 0.080	9.49 ± 0.105	0.31
C. nutti PRE	1.45	0.70 ± 0.048	0.57 ± 0.039	1.27 ± 0.087	1.23
C. njegovanae	1.36	0.60 ± 0.044	9.55 ± 0.702	10.15 ± 0.746	0.06
R. frigida	3.56	0.31 ± 0.009	14.78 ± 0.415	15.09 ± 0.424	0.02

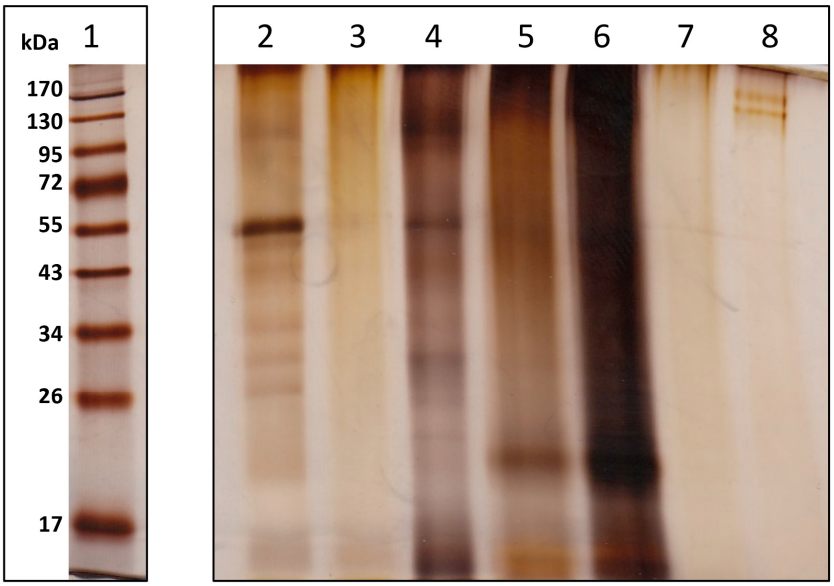

Figure 8. SDS-PAGE of skeletal organic matrices. Lane 1: Molecular weight markers, from up to down: 170, 130, 95, 72, 55, 43, 34, 26 and 17 kDaltons. Lanes 2–4 *Cellarinella nutti*: 2. ASM (10 µL), 3. PRE-ASM (20 µL); 4. LS-AIM (10 µL). Lanes 5–6 *Cellarinella njegovanae*: 5. ASM (20 µL), 6. LS-AIM (10 µL); Lanes 7–8 *Reteporella frigida*: 7. ASM (10 µL), 8. LS-AIM (20 µL). ASM: Acid-soluble matrix. LS-AIM: Laemmli-soluble acid-insoluble matrix. PRE= pre-bleached. Loaded solutions: 10 or 20 µL.

3.2.2. FT-IR Spectroscopy

FT-IR spectra are shown on Figure 9. The spectra of all tested skeletal powders characterized calcite, with a low amplitude single absorption band at 713 cm^{-1}, a sharp high amplitude band at 877 cm^{-1} and a large band at 1429 cm^{-1}. We found for none of the tested samples the 700–713 cm^{-1} doublet or the 858, 1083 and 1477 cm-1 absorption bands that are characteristic for aragonite. Because of low quantities of ASM lyophilized extracts and the difficulty in handling them, only AIMs were analyzed by this technique. In the 2500–4000 cm^{-1} range, all samples exhibited one broad band located at 3290–3350 cm^{-1}, which was usually attributed to the amide A group [ν(N − H)] and a double absorption band at 2921/23–2854/51 cm^{-1}, generally assigned to the ν(C − H) stretching vibrations (carbohydrates, lipids). In addition, all spectra exhibited the presence of amide absorption bands at 1647/52 and 1542/60 cm^{-1}, ascribed to the amide I [ν(C = O)] and II [ν(C − N)] bands, respectively. This combination typically characterizes the protein moieties. A large absorption band of high amplitude around 1022–1026–1080 cm^{-1} was assigned to carbohydrate moieties (stretching vibrations). Below 800 cm^{-1}, other absorption bands of low amplitude were also observed, but their precise assignation will require further investigations.

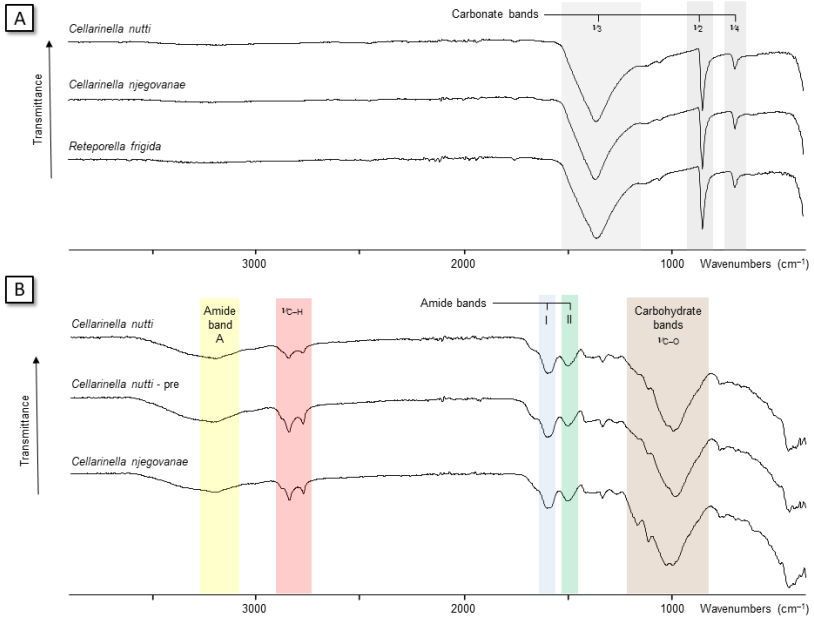

Figure 9. FT-IR spectra: (**A**) clean skeletal powder of *Cellarinella nutti, Cellarinella njegovanae* and *Reteporella frigida*; (**B**) acid Insoluble Matrix (AIM) of *C. nutti, C. nutti* PRE and *C. njegovanae.* PRE = pre-bleached. The absorption bands corresponding to identified functions are highlighted in color.

3.2.3. ELLA Test

The enzyme-linked lectin assays (ELLA) determined the types of glycan structures present in ASM extracts of the three Antarctic bryozoan species. Specifically, this technique allowed a species-specific "lectin signature" to be obtained [65,66]. The results, expressed as percentages of reactivity with respect to the most reactive lectin for each species, are given in Figure 10A–C. The lectin reactivities are classified in three groups: strong reactivity: >60%; moderate reactivity: between 20 and 60%; weak reactivity or close to 0: <20%. The reactivity pattern obtained with *Reteporella frigida* ASM was relatively simple: the most reacting lectins were LEL, STL Jacalin WGA and DSL. The reactivities of these lectines are often related because they recognize different sugar motifs comprising N-acetylglucosamine or oligomers of this monosaccharide. As consequence, they are considered as "chitin-binding" lectins, in the broad sense. Jacalin is a α-D galactose-binding lectin, which also recognizes N-acetylgalactosamine. Besides being highly specific of the T-antigen, Jacalin is often used as a marker of O-linked glycoproteins. In addition to these lectins, ConA and RCA exhibited a low reactivity (around 30%); ConA is a mannose-binding lectin and has affinity to N-linked glycopeptides while RCA binds to β-galactose. All the other lectins were almost unreactive to the *R. frigida* ASM extract. The lectin reactivity patterns obtained with the two *Cellarinella* species were more complex, since more lectins gave a moderate to high reactivity. For *Cellarinella nutti*, the most reactive lectin was Jacalin. LEL, STL and WGA (chitin-binding) showed high reactivity in addition to VVA, an N-acetyl-D-galactosamine binding lectin that preferably binds monomer of this sugar connected to serine or threonine (O-glycosidic linkage). ConA, SBA, RCA, and PNA gave relatively strong reactivities; SBA and PNA are often associated since they both recognize galactose, and SBA exhibits a strong affinity to N-acetyl-D-galactosamine. LCA, SJA, PSA, UEA-I, DBA, succinylated WGA, PHA-E and DSL (in this decreasing order) displayed moderate reactivity. ECL, GSL-II, and PHA-L were unreactive. The reactivity pattern of *Cellarinella njegovanae* exhibited some similarities with that of *C. nutti*, but it was not superimposable. Among the most reactive lectins found were WGA, Jacalin, STL, LEL, RCA, DSL, GSL-I and succinylated WGA, all largely above 60% reactivity. ConA and WGA showed reactivities close to this threshold value. SBA, LCA, PNA, PSA, UEA-I, DBA, SJA and PHA-E exhibited moderate reactivities. Similarly

to *C. nutti*, ECL, PHA-L, GSL-II were practically unreactive. The important differences between the lectin reactivity patterns of *C. nutti* and *C. njegovanae* encompassed mainly two lectins: succinylated WGA and DSL, whose reactivity levels were high in *C. njegovanae* and very low in *C. nutti*. Other differences affected WGA, RCA and GSL-I, whose reactivities were higher in *C. njegovanae* than in *C. nutti.* Some of these differences might be explained by biochemistry (see Discussion section).

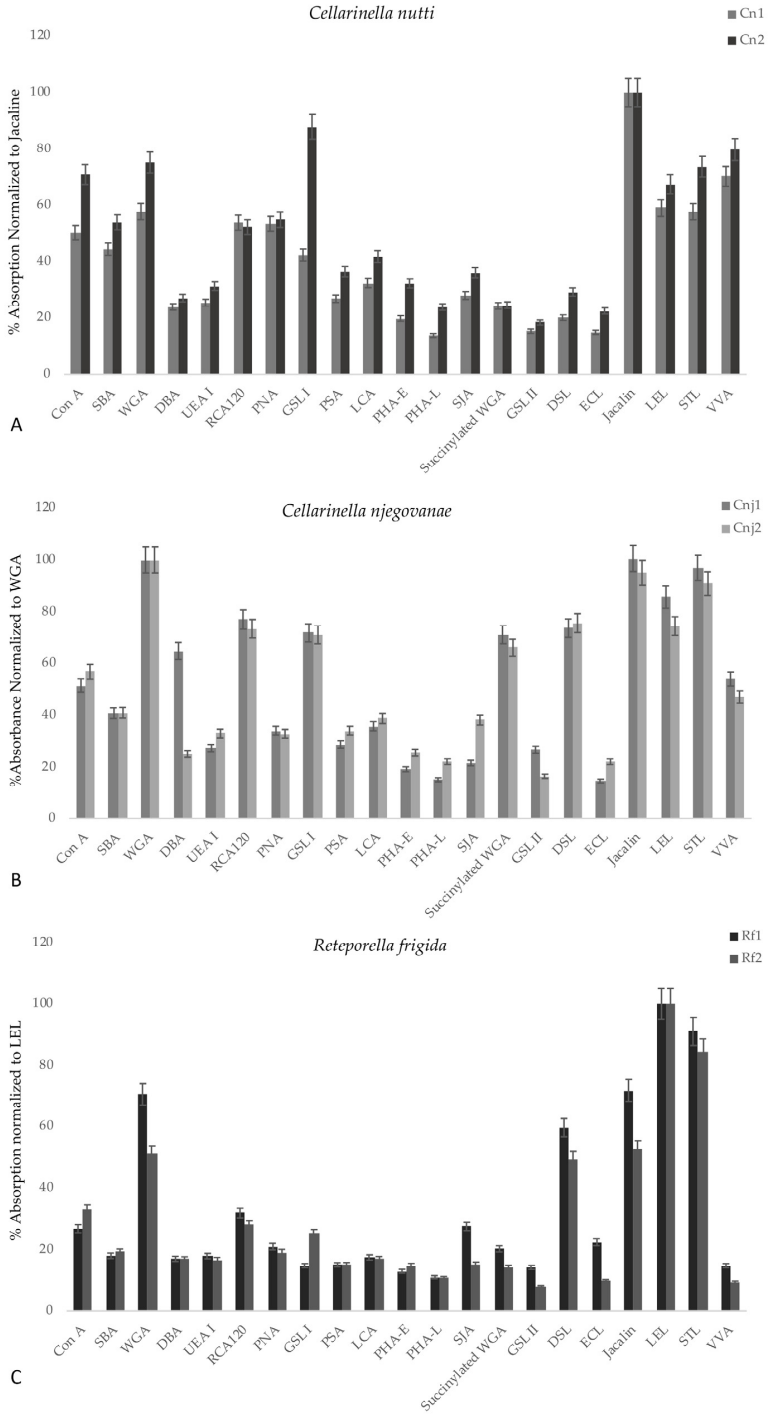

Figure 10. Enzyme-linked lectin assay (ELLA) on the three extracted ASMs. ELLA was performed with 21 lectins tested on: (**A**) *Cellarinella nutti*, (**B**) *Cellarinella njegovanae* and (**C**) *Reteporella frigida*. One and two are replicates. Absorbance values at 405 nm were normalized to the highest values (Jacalin, WGA and LEL), corresponding to 100% reactivity (n = 4, mean ± S.E.), for *C. nutti* (**A**), *C. njegovanae* (**B**) and *R. frigida* (**C**), respectively.

3.3. Sea-Water Characteristics and Isotopy

Temperature at Site 1 in November 2018 was −1.57 ± 0.03 °C (−1.67 to −1.38 °C), salinity 34.74 ± 0.005 PSU (34.72 to 34.76 PSU), conductivity 27.53 ± 0.03 mS/cm (27.44 to 27.68 mS/cm), dissolved oxygen 7.37 ± 0.07 mL/L (7.17 to 7.71 mL/L), density 1028.07 ± 0.01 kg/m^3 (1028.04 to 1028.09 kg/m^3) and pH 8.06 ± 0.01 (8.04 to 8.10). All this data is reported as average with ±1 standard deviation and with ranges in brackets.

At this site, seawater sample 2A (Lab-code W-19824) yielded a $\delta^{18}O_{sw}$ of −0.59‰ VSMOW and a $\delta^{2}H_{sw}$ of −5.09‰ VSMOW. Dissolved inorganic carbon (DIC) and carbon isotopes of sample 2A (Lab-code C-12599) yielded $\delta^{13}C_{DIC}$ of 1.06 ± 0.03‰ VPDB and a DIC concentration of 2.26 ± 0.05 mmol/L.

4. Discussion

An integrated approach—encompassing morphological description, biomineralization via the analysis of the skeletal components, and environmental geochemical characterization—is here applied for the first time to three Antarctic bryozoans from Terra Nova Bay (Ross Sea).

To our current knowledge, over 95% of the bioconstructional bryozoan species of the SO are distributed only on the Antarctic shelf (0–1000 m depth). Recent campaigns in the Ross Sea [13] revealed a dominance of calcified bioconstructional bryozoans between 250 and 900 m deep on the Ross Sea banks (Pennel Banks and Ross Sea Platform), with *Cellarinella* Waters, 1904, *Lageneschara* Hayward &Thorpe, 1988, *Thrypticocyrrus* Hayward & Thorpe, 1988 and *Pemmatoporella* Hayward & Taylor, 1984 as the principal genera. Shallow and deep sites of Tethys Bay were mostly characterized by *Cellarinella* (*Cellarinella nutti* Rogick, 1956 *Cellarinella njegovanae* Rogick, 1956) and *Reteporella* (*Reteporella frigida* Waters, 1904) as bioconstructional species that, together with sponges, cold-water corals, mollusks, hydroids etc. form structurally complex calcifying ecosystems. Although still poorly known, morphological, structural, and metabolic responses of such ecosystems are likely influenced by the spatial and temporal variability of seasonal ice scour, carbonate chemistry and primary productivity [44].

During summer months, the variability of the surface carbonate system's properties at the shallow site in Tethys Bay is primarily controlled by biological activities [49,50]. When the ice melts, normally in December [50], it influences the carbonate system chemistry, acting both directly, through dilution processes, and indirectly, by favoring the development of phytoplankton blooms [46]. In such conditions, bryozoans as well as other suspension feeders receive an abundant supply of food in a few hours. In response, colonies firstly increase their feeding rate [55,56] (i.e., food as source of energy for the colony) and then invest in colony growth and reproduction, as confirmed by the morphometric traits of both *Cellarinella* species. The widest primary orifices were found in zooids at the proximal and middle part of each band in *C. nutti* and *C. njegovanae*, respectively (Table S1). Wider orifices imply increased colony investment to feeding zooids, which are the major players for reactivating colony metabolism after winter dormancy [55,56]. The difference observed between the two species could be explained by a delay in food availability between the two depths, requiring a quicker response for the shallow species than the deeper one.

The shift between high productivity in the summer and heterotrophy in the winter is confirmed by the growth banding patterns found in all colonies of the two *Cellarinella* species. Such changes in environmental conditions, determining the slow growth and the longevity of these Antarctic bryozoans [72], also affect carbonate deposition [34,35,73] in calcifying structures. This is evident from the differences among band lengths (see Table 2). Even though no relationship between band length and zooidal length (Tables 2 and S1) was observed, newly formed zooids of the year differed in morphometric traits between the two species. Located at the proximal part of each band, these new zooids were the shortest of the band in *C. nutti* but the longest of the band in *C. njegovanae* (Table S1). These observations confirm that, after the winter period, *C. nutti* colonies invest in budding new feeding zooids (i.e., shortest zooids with widest orifices), whereas in *C. njegovanae* colonies growing below 100 m, colonies prioritize zooidal growth (i.e., widest orifice in the middle part of the band).

These preliminary results pose interesting questions regarding the plastic potential of the two Antarctic species, already observed in other bryozoan species [74–76]. Future in situ studies will be required to evaluate the vulnerability or resilience (i.e., adaptability) of Antarctic bryozoans under the fast-occurring current climate change in polar areas.

Calcitic bryozoans are dominant in Antarctica [77,78], but they lack the mineralogical variability generally characterizing the phylum [79]. In fact, the three bioconstructional species are entirely calcitic with low $MgCO_3$ contents (<4 mol%). Observations and measurements on zooidal walls using micro-CT analyses confirmed an investment of *Cellarinella* species in mineralization during wintertime through the thickening of both lateral and basal walls (see Table 3). Even though the colonies seem to be inactive, the calcification processes do not stop during winter. The thickening of the basal and lateral walls occurring during this period is two to five times more than that occurring in spring, summer and autumn (See Rbwgcl/bwgb for both species). The ability shown by *Cellarinella* colonies to allocate energy resources from feeding activities, budding, reproduction and growth (in summer) to mineralization (i.e., skeletal thickening) (in winter) indicates a high plasticity [76]. Among all metabolic processes, biomineralization is the only one which seems to persist throughout the year, and especially during the Antarctic winter. A different behavior was shown by *Reteporella frigida*, whose zooids displayed basal and lateral wall thickening in some colony portions (i.e., around the fenestrule) more related to a structural thickening (see Figure 7). The colonies are characterized by convoluted and fenestrated laminae, promoting habitat complexity [8], but that have to cope with strong current conditions. Unlike the two *Cellarinella* species, *Reteporella frigida* attaches on the rocky substrate with an encrusting base; thus, its rigid colony structure has to resist the force of the currents.

After having been in the shadow of more accessible organisms (like sponges) for a long time, bryozoans are now catalyzing interest for their bioactive metabolites [80], molecules obtained from the soft tissues [81,82]. Particularly useful in pharmacology, bryostatins (macrolactones) extracted from *Bugula neritina* are chemotherapeutic agents, i.e., molecules of interest for the treatment of cancers. The innovative part of this study is the characterization of the organic matrix associated with the skeletal tissues (SOM). In our protocol, given the porous nature of bryozoan skeletal tissues, we extracted only macromolecular components strongly linked to the mineral phase (i.e., intra-crystalline molecules). To this end, we applied a two-step harsh cleaning procedure with sodium hypochlorite to remove non-skeletal components and other contaminants, thus ensuring that only molecules involved in the mineral deposition were analyzed [83].

Even though the extraction and the preliminary characterization of SOM components is novel for bryozoans, comparisons can be made with other calcifying phyla. The different extracts studied here exhibit numerous biochemical characteristics that are similar to those of calcified tissues in other metazoans. As quantities, the percentage of SOM ranged from 0.1% (*C. nutti*) to almost 0.75% (*C. njegovanae*) of the skeletal powder, values comparable with those characterizing several mollusc shells [84]. Interestingly, the insoluble to soluble ratio varies significantly in our extracts, but such variations have amplitudes similar to those detected in mollusc shells. In pearl oyster nacre, the insoluble to soluble matrix ratio ranges from 20 to 50 [85], meaning that nacre SOM is mainly composed of insoluble macromolecules, while the AIM/ASM ratio is about five in the crossed-lamellar queen conch [86]. A very interesting aspect is the high variation of the ratio found within the genus *Cellarinella* (0.3 in *C. nutti* vs. 0.06 for *C. njegovanae*) and, even more, within *C. nutti* (0.3 in *C. nutti* vs. 1.2 in *C. nutti* PRE). Such large variations have not been observed in mollusc shells belonging to the same clade. A possible explanation is that skeletal matrices of closely related specimens, while containing supposedly similar macromolecules, may be prone to different levels of "cross-linking" when they are synthesized. "Cross-linking" is the process converting soluble into insoluble macromolecules, forming intermolecular bonds. But this hypothesis will require further investigations, in particular via proteomics.

Other similarities with the matrices associated with calcium carbonate biominerals are observed via FTIR and SDS-PAGE analyses. For FTIR, the IR spectra of the insoluble

matrices contain the two amide absorption bands (I, II), corresponding to the proteins. The AIMs are also characterized by a large absorption band between 1020–1080 cm^{-1}, corresponding to carbohydrates. Thus, bryozoan matrices are a mixture comprising proteins and polysaccharides, similar to other skeletal matrices. The SDS-PAGE profiles show that each extract comprises a mix between smearing (i.e., non-discrete, macromolecules that constitute the background of the lanes) and molecules of discrete molecular weights, with blurred and thickened bands. In addition, some of the extracts tend to stain poorly with silver nitrate or even to stain negatively. All these characteristics on gel typify matrices associated to the calcium carbonate biominerals [87].

In addition, the "lectin fingerprint" of each extract has been obtained for the first time. The lectin fingerprint of *Reteporella frigida* differs from those of *Cellarinella* species. Despite the differences, all three lectin fingerprints have in common high reactivity to LEL, STL and WGA lectins. This suggests that they all contain chitin—a polymer of N-acetyl glucosamine—or saccharides that resemble chitin. In bryozoans, chitin has been very poorly studied. To our knowledge, only two papers refer to chitin in bryozoans: the first evidencing chitin as a component of the organic non-mineralized exoskeleton in *Flustra foliacea* [88], and the second isolating and characterizing chitin in the freshwater, non-mineralized bryozoan *Plumatella repens* [89]. Therefore, our finding strongly suggests that chitin or chitin-like saccharides are true components of the SOM, together with proteins. It is interesting to note that we only analyzed the soluble part of the SOM, whereas the insoluble moieties were inaccessible to the ELLA test. In standard conditions, chitin is insoluble (by "cross-linking"), thus polymers evidenced by LEL, STL or WGA might represent either a particular soluble form of chitin, or chitin fragments. In this second case, these fragments might be the result of a partial hydrolysis of true chitin following the bleach treatment, or soluble oligomers of chitin or chitin-like saccharides, or all three possibilities together.

More generally, the presence of chitin in calcium carbonate biominerals has been long debated. In mollusc shells, chitin has been detected only a few times [90,91] due to the difficulty in obtaining direct experimental evidence of its presence, especially if chitin is a minor component of a sclerotized protein-saccharide mixture. Chitin is indirectly detected as a component of the skeletal matrix. Its detection can occur via its conversion to chitosan, via a mild hydrolysis releasing monomers of N-acetyl glycosamine, or via its ability to be targeted by chitin-binding lectins, as shown in the present work. More directly, proteomic analyses of the skeletal matrix components show the presence of enzymes involved in chitin metabolism—and remodeling (chitin synthase, chitinase)—or proteins that exhibit chitin-binding motifs, suggesting the presence of this sugar polymer in a calcified matrix [92]. From "classical knowledge" on mollusc shell formation, chitin is supposed to be a universal polymer in every shell. However, this view has been challenged by recent work [93] using solid state NMR showing chitin to be a minor component or completely absent from some shells. The presence of chitin in the calcified skeletons of bryozoans is a matter for further investigations, as explained above, using different experimental methods. Another interesting conclusion from the ELLA results concerns the lectin fingerprints of the two *Cellarinella* species, which are very similar but also exhibit striking differences. The fact that *C. njegovanae* ASM reacts with WGA and succinylated WGA whereas *C. nutti* only reacts with WGA may have a biochemical explanation. WGA is generally considered as a "chitin-binding lectin" (it binds preferentially to dimers or trimers of N-acetyl-glucosamine) also exhibiting a strong affinity with sialic acid. On the contrary, succinylated WGA has a binding activity restricted to N-acetyl-glucosamine-containing motifs and never binds to sialic acid. A high level of succinylated WGA in *C. njegovanae* and a low level in *C. nutti* suggests that all the binding sites of WGA/succinylated WGA in *C. njegovanae* are predominantly of the "chitin" type rather than of the sialic acid type, even though an important percentage of the motifs recognized by WGA in *C. nutti* consists of sialic acid. In other words, the difference strongly suggests that the *C. nutti* ASM may be much more sialylated than the *C. njegovanae* ASM. This hypothesis needs to be confirmed by a very precise quantification of sialic acid in the extracts though spectrofluorometric methods.

Once more, our data emphasize the putative important role of sialic acids, a class of sugars that is widely neglected in the biomineralization community.

These observation and preliminary analyses raise interesting questions how environmental factors drive biomineralization processes in bryozoans at molecular and also macrostructural (i.e., zooidal and colonial) levels. Our preliminary results show that in November 2018, seawater conditions at the shallow site were representative of summer conditions with bottom water temperatures slightly higher than the reported winter minima of around −1.8 °C for Tethys Bay between November 2018 and November 2019 [50]. The oxygen isotope composition measured in November 2018 ($\delta^{18}O_{sw}$ of −0.59 ‰) fell outside the $\delta^{18}O_{sw}$-range (−0.47 to −0.04‰ VSMOW) for Antarctic surface water and high salinity shelf water measured in austral summers 1987/88 and 1989/90 of Terra Nova Bay [93]. Therefore, this decrease in $\delta^{18}O_{sw}$ was a clear indication of increased meltwater contribution along the coast of Victoria Land, which leads to a freshening of the Western Ross Sea. This is consistent with the freshening trend already described in the Southern Ross Sea [94] across recent decades. The pH value recorded at Site 1 (8.06) coincided with low values at the beginning of the summer season prior to the onset of plankton blooms and a concomitant pH-increase between November 2018 and November 2019 [50]. Break-up of the pack-ice in spring (December) in the bay leads to light availability and a strong temperature increase which peaks in January-February, boosting benthic life and consequently to a seasonal decrease in dissolved inorganic carbon (DIC). The recorded value for the shallow site (2.26 ± 0.05 mmol/L) marked the onset of spring, with presumably lowered values during summer, analogous to the seasonal pattern reported for McMurdo Sound [95]. Carbon isotopes are expected to vary strongly with seasonal biological activities, which include not only phytoplankton blooms, changes in species composition depending on sea ice influence, current, and water mixing [51], but also physiological processes of bacteria [52] and, on a macro scale, of benthic ecosystems (i.e., respiration, photosynthesis, calcification). But for the moment there are no comparative values available from Terra Nova Bay, and our shallow water $\delta^{13}C_{DIC}$ (1.06 ± 0.03 ‰ VPDB) marked the onset of the season.

Understanding the processes of skeleton formation, from molecular to macro structures, is a key aspect of comprehending the adaptation of bioconstructional ecosystems in the future ocean. This work paves the way for studying complex organisms like bryozoans, and especially for investigating their biomineralization process. In the near future, we plan to employ high-throughput techniques, including transcriptomics and proteomics, to identify the numerous molecular actors involved in biomineral deposition in bryozoans.

Supplementary Materials: The following are available online at https://www.mdpi.com/article/10.3390/min13020246/s1. Table S1 Zooid morphometrics of *Cellarinella nutti*, *Cellarinella njegovanae* and *Reteporella frigida*. When present, number of bands are reported per colony per species. Measurements of zooid length and orifice width (n = 30) are reported per each position within the band and as mean values for each band.

Author Contributions: Conceptualization, C.L. and F.M.; methodology, C.L., F.M., P.K., G.R., A.B., E.S. and G.B.; software, C.L., F.M., C.M., M.L.C., R.v.G., L.P. and J.T; validation C.L., F.M. and P.K.; formal analysis C.L., F.M., C.M. and M.L.C.; investigation, C.L., F.M., C.M., M.L.C., R.v.G., L.P. and J.T.; resources, C.L., P.K., G.R., A.B., E.S. and G.B.; data curation, C.L., F.M., C.M. and M.L.C.; writing—original draft preparation, C.L. and F.M.; writing—review and editing, C.L., F.M., C.L., M.L.C., P.K. and R.v.G.; visualization, C.L., P.K., G.R., A.B., E.S. and G.B.; supervision, C.L., F.M. and P.K.; project administration, C.L.; funding acquisition, C.L. and F.M. All authors have read and agreed to the published version of the manuscript.

Funding: This research was funded by the National Antarctic Research Program (PNRA, Italy), grant number PNRA 2016/AZ1.09 to C.L. Complementary funding for SOM analysis was provided to F.M. via MC-COBRA project (2019–2020), financed by the University of Burgundy through the "BQR-Recherche en Réseau 2019" yearly program. CNR-ISMAR Bologna scientific contribution #2040 to M.L.C.

Data Availability Statement: Raw data on zooid morphometrics, microCT and ELLA test have been stored in ZENODO: https://zenodo.org/record/7584660#.Y9es7y9aYh8 (accessed on 10 January 2023). https://doi.org/10.5281/zenodo.7584660.

Acknowledgments: The authors would like to thank all colleagues of XXXIV and XXXV Italian Expeditions to Antarctica for the technical and scientific support. A special thanks to COMSUBIN Navy Divers and the logistic staff of Mario Zucchelli Station. The authors acknowledge Paul D. Taylor for revising the manuscript and the two anonymous reviewers for their valuable comments.

Conflicts of Interest: The authors declare no conflict of interest. The funders had no role in the design of the study; in the collection, analyses, or interpretation of data; in the writing of the manuscript; or in the decision to publish the results.

References

1. Taylor, P.D. *Bryozoan Paleobiology*; John Wiley & Sons: Hoboken, NJ, USA, 2020.
2. Zhang, Z.; Zhang, Z.; Ma, J.; Taylor, P.D.; Strotz, L.C.; Jacquet, S.M.; Skovsted, C.B.; Chen, F.; Han, J.; Brock, G.A. Fossil evidence unveils an early Cambrian origin for Bryozoa. *Nature* **2022**, *599*, 251–255. [CrossRef] [PubMed]
3. Hughes, R.N. Lessons in modularity: The evolutionary ecology of colonial invertebrates. *Sci. Mar.* **2005**, *69*, 169–179. [CrossRef]
4. Carroll, S.B. Chance and necessity: The evolution of morphological complexity and diversity. *Nature* **2001**, *409*, 1102–1109. [CrossRef]
5. Ma, J.; Taylor, P.D.; Xia, F.; Zhan, R. The oldest known bryozoan: *Prophyllodictya* (Cryptostomata) from the lower Tremadocian (Lower Ordovician) of Liujiachang, south-western Hubei, central China. *Palaeontology* **2015**, *58*, 925–934. [CrossRef]
6. Taylor, P.D.; Lombardi, C.; Cocito, S. Biomineralization in bryozoans: Present, past and future: Bryozoan biomineralization. *Biol. Rev.* **2015**, *90*, 1118–1150. [CrossRef] [PubMed]
7. Wray, G.A. Molecular clocks and the early evolution of metazoan nervous systems. *Philos. Trans.* **2015**, *370*, 20150046. [CrossRef]
8. Wood, A.C.L.; Probert, P.K.; Rowden, A.; Smith, A. Complex habitat generated by marine bryozoans: A review of its distribution, structure, diversity, threats and conservation. *Aquat. Conserv. Mar. Freshw. Ecosyst.* **2012**, *22*, 547–563. [CrossRef]
9. Taylor, P.D.; Kudryavtsev, A.B.; Schopf, J.W. Calcite and aragonite distributions in the skeletons of bimineralic bryozoans as revealed by Raman spectroscopy. *Invertebr. Biol.* **2008**, *127*, 87–97. [CrossRef]
10. Hiscock, K. *Marine Biodiversity Conservation, a Practical Approach*; Earthscan from Routledge (Taylor and Francis Group): London, UK; New York, NY, USA, 2014; p. 298.
11. Cocito, S.; Novosel, M.; Novosel, A. Carbonate bioformations around underwater freshwater springs in the north-eastern Adriatic Sea. *Facies* **2004**, *50*, 13–17. [CrossRef]
12. Lombardi, C.; Cocito, S.; Taylor, P.D. Bryozoan Bioconstructions in a Changing Mediterranean Sea. In *The Mediterranean Sea—Its History and Present Challenges*; Goffredo, S., Dubinsky, Z., Eds.; Springer: New York, NY, USA, 2013; pp. 373–384.
13. Lombardi, C.; Taylor, P.D.; Cocito, S. Bryozoans: The Forgotten Bioconstructors. In *Perspective on the Marine Animal Forest*; Rossi, S., Bramanti, L., Eds.; Springer Nature: Berlin, Germany, 2021; Volume 11, pp. 193–217.
14. Meredith, M.P.; Schofield, O.; Newman, L.; Urban, E.; Sparrow, M. The vision for a Southern Ocean Observing System. *Curr. Opin. Environ. Sustain.* **2013**, *5*, 306–313. [CrossRef]
15. Meredith, M.P.; Sommerkorn, M.; Cassotta, S.; Derksen, C.; Ekaykin, A.; Hollowed, A.; Kofinas, G.; Mackintosh, A.; Mel-bourne-Thomas, J.; Muelbert, M.M.C.; et al. *IPCC Special Report on the Ocean and Cryosphere in a Changing Climate*; Pörtner, H.-O.D.C., Roberts, V., Masson-Delmotte, P., Zhai, M., Tignor, E., Poloczanska, K., Mintenbeck, A., Alegría, M., Nicolai, A., Okem, J., et al., Eds.; Intergovernmental Panel on Climate Change: Geneva, Switzerland, 2019.
16. Deppeler, S.L.; Davidson, A.T. Southern Ocean Phytoplankton in a Changing Climate. *Front. Mar. Sci.* **2017**, *4*, 40. [CrossRef]
17. Caldeira, K.; Duffy, P.B. The Role of the Southern Ocean in Uptake and Storage of Anthropogenic Carbon Dioxide. *Science* **2000**, *287*, 620–622. [CrossRef]
18. Sabine, C.L.; Feely, R.A.; Gruber, N.; Key, R.M.; Lee, K.; Bullister, J.L.; Wanninkhof, R.; Wong, C.S.; Wallace, D.W.R.; Tilbrook, B.; et al. The Oceanic Sink for Anthropogenic CO_2. *Science* **2004**, *305*, 367–371. [CrossRef] [PubMed]
19. Convey, P.; Peck, L.S. Antarctic environmental change and biological responses. *Sci. Adv.* **2019**, *5*, eaaz0888. [CrossRef]
20. Barnes, D.K.A. Iceberg killing fields limit huge potential for benthic blue carbon in Antarctic shallows. *Glob. Chang. Biol.* **2016**, *23*, 2649–2659. [CrossRef] [PubMed]
21. Barnes, D.K.A. Polar zoobenthos blue carbon storage increases with sea ice losses, because across-shelf growth gains from longer algal blooms outweigh ice scour mortality in the shallows. *Glob. Chang. Biol.* **2017**, *23*, 5083–5091. [CrossRef]
22. Gutt, J.; Isla, E.; Bertler, A.; Bodeker, G.; Bracegirdle, T.; Cavanagh, R.; Comiso, J.; Convey, P.; Cummings, V.; De Conto, R.; et al. Cross-disciplinarity in the advance of Antarctic ecosystem research. *Mar. Genom.* **2017**, *37*, 1–17. [CrossRef]
23. Henley, S.F.; Schofield, O.M.; Hendry, K.R.; Schloss, I.R.; Steinberg, D.K.; Moffat, C.; Peck, L.S.; Costa, D.P.; Bakker, D.C.; Hughes, C.; et al. Variability and change in the west Antarctic Peninsula marine system: Research priorities and opportunities. *Prog. Oceanogr.* **2019**, *173*, 208–237. [CrossRef]
24. Gutt, J.; Starmans, A. Structure and biodiversity of megabenthos in the Weddell and Lazarev Seas (Antarctica): Ecological role of physical parameters and biological interactions. *Polar Biol.* **1998**, *20*, 229–247. [CrossRef]

25. Parker, S.J.; Bowden, D.A. Identifying taxonomic groups vulnerable to bottom longline fishing gear in the Ross Sea region. *CCAMLR Sci.* **2010**, *17*, 105–127.
26. Barnes, D.K.A.; Downey, R.V. Bryozoa. In *Biogeographic Atlas of the Southern Ocean*; De Broyer, C., Koubbi., P., Griffiths, H.J., Raymond, B., Udekem d'Acoz, C.d., Eds.; SCAAR: Cambridge, UK, 2014; pp. 195–199.
27. De Broyer, C.; Danis, B. How many species in the Southern Ocean? Towards a dynamic inventory of the Antarctic marine species. *Deep. Sea Res. Part II* **2011**, *58*, 5–17. [CrossRef]
28. Figuerola, B.; Gordon, D.P.; Polonio, V.; Cristobo, J.; Avila, C. Cheilostome bryozoan diversity from the Southwest Atlantic region: Is Antarctica really isolated? *J. Sea Res.* **2014**, *85*, 1–17. [CrossRef]
29. Rosso, A. Bryozoa from Terra Nova Bay (Ross Sea, Antarctica). In *Oceanografia in Antartide*; Gallardo, V.A., Ferretti, O., Moyano, H.I., Eds.; Universidad de Concepcion: Centro Eula, Chile, 1992; pp. 359–369.
30. Pabis, K.; Hara, U.; Presler, P.; Sicinski, J. Structure of bryozoan communities in an Antarctic glacial fjord (Admiralty Bay, South Shetlands). *Polar Biol.* **2014**, *37*, 737–751. [CrossRef]
31. Figuerola, B.; Hancock, A.M.; Bax, N.; Cummings, V.J.; Downey, R.; Griffiths, H.J.; Smith, J.; Stark, J.S. A Review and Meta-Analysis of Potential Impacts of Ocean Acidification on Marine Calcifiers from the Southern Ocean. *Front. Mar. Sci.* **2021**, *8*, 584445. [CrossRef]
32. Eggleston, D. The Marine Polyzoa of the Isle of Man. Ph.D. Thesis, University of Liverpool, Liverpool, UK, 1963; pp. 1–297.
33. Bader, B.; Schäfer, P. Skeletal morphogenesis and growth check lines in the Antarctic bryozoan *Melicerita obliqua*. *J. Nat. Hist.* **2004**, *38*, 2901–2922. [CrossRef]
34. Smith, A.M.; Stewart, B.; Key, M.M., Jr.; Jamet, C.M. Growth and carbonate production by *Adeonellopsis* (Bryozoa: Cheilostomata) in Doubtful Sound, New Zealand. *Palaeogeogr. Palaeoclimatol. Palaeoecol.* **2001**, *175*, 201–210. [CrossRef]
35. Barnes, D.K. Seasonal and annual growth in erect species of Antarctic bryozoans. *J. Exp. Mar. Biol. Ecol.* **1995**, *188*, 181–198. [CrossRef]
36. Barnes, D.; Webb, K.; Linse, K. Slow growth of Antarctic bryozoans increases over 20 years and is anomalously high in 2003. *Mar. Ecol. Prog. Ser.* **2006**, *314*, 187–195. [CrossRef]
37. Barnes, D.K.A.; Webb, K.E.; Linse, K. Growth rate and its variability in erect Antarctic bryozoans. *Polar Biol.* **2007**, *30*, 1069–1081. [CrossRef]
38. Tavener-Smith, R.; Williams, A. The secretion and structure of the skeleton of living and fossil Bryozoa. *Philos. Trans. R. Soc. London B Biol. Sci.* **1972**, *264*, 97–160. [CrossRef]
39. Lowenstam, H.A.; Weiner, S. *On Biomineralization*; Oxford University: Oxford, UK, 1989.
40. Dove, P.M.; deYoreo, J.J.; Weiner, S. Biomineralization. *Rev. Min. Geochem.* **2003**, *54*, 1–381.
41. Marin, F.; Bundeleva, I.; Takeuchi, T.; Immel, F.; Medakovic, D. Organic matrices in metazoan calcium carbonate skeletons: Composition, functions, evolution. *J. Struct. Biol.* **2016**, *196*, 98–106. [CrossRef]
42. Barnes, D. Antarctic sea ice losses drive gains in benthic carbon drawdown. *Curr. Biol.* **2015**, *25*, R789–R790. [CrossRef] [PubMed]
43. Peck, L.S.; Barnes, D.K.A.; Coock, A.J.; Fleming, A.H.; Clarke, A. Negative feedback in the cold: Ice retreat produces new carbin sink in Antarctica. *Glob. Chang. Biol.* **2010**, *16*, 2614–2623. [CrossRef]
44. Santagata, S.; Ade, V.; Mahon, A.R.; Wisocki, P.A.; Halanych, K.M. Compositional Differences in the Habitat-Forming Bryozoan Communities of the Antarctic Shelf. *Front. Ecol. Evol.* **2018**, *6*, 116. [CrossRef]
45. Illuminati, S.; Annibaldi, A.; Romagnoli, T.; Libani, G.; Antonucci, M.; Scarponi, G.; Totti, C.; Truzzi, C. Distribution of Cd, Pb and Cu between dissolved fraction, inorganic particulate and phytoplankton in seawater of Terra Nova Bay (Ross Sea, Antarctica) during austral summer 2011–12. *Chemosphere* **2017**, *185*, 1122–1135. [CrossRef]
46. Budillon, G.; Pacciaroni, M.; Cozzi, S.; Rivaro, P.; Catalano, G.; Ianni, C.; Cantoni, C. An optimum multiparameter mixing analysis of the shelf waters in the Ross Sea. *Antarct. Sci.* **2003**, *15*, 105–118. [CrossRef]
47. Nihashi, S.; Ohshima, K.I. Circumpolar Mapping of Antarctic Coastal Polynyas and Landfast Sea Ice: Relationship and Variability. *J. Clim.* **2015**, *28*, 3650–3670. [CrossRef]
48. Faranda, F.M.; Guglielmo, L.; Ianora, A. The Italian Oceanographic Cruises in the Ross Sea (1987-95): Strategy, General Consideration Description of the Sampling Sites. In *Ross Sea Ecology*; Faranda, F.M., Guglielmo, L., Ianora, A., Eds.; Springer: Berlin/Heidelberg, Germany, 2000; pp. 1–14.
49. Silvano, A.; Foppert, A.; Rintoul, S.R.; Holland, P.R.; Tamura, T.; Kimura, N.; Castagno, P.; Falco, P.; Budillon, G.; Haumann, F.A.; et al. Recent recovery of Antarctic Bottom Water formation in the Ross Sea driven by climate anomalies. *Nat. Geosci.* **2020**, *13*, 780–786. [CrossRef]
50. Lombardi, C.; Kuklinski, P.; Bordone, A.; Spirandelli, E.; Raiteri, G. Assessment of Annual Physico-Chemical Variability via High-Temporal Resolution Monitoring in an Antarctic Shallow Coastal Site (Terra Nova Bay, Ross Sea). *Minerals* **2021**, *11*, 374. [CrossRef]
51. Pusceddu, A.; Dell'Anno, A.; Fabiano, M. Organic matter composition in coastal sediments at Terra Nova Bay (Ross Sea) during summer. *Polar Biol.* **2000**, *23*, 288–293. [CrossRef]
52. Alonso-Saez, L.; Sanchez, O.; Gasol, J.; Balaguè, V.; Pedros-Alio, C. Winter-to-summer changes in the composition and sin-gle-cell activity of near-surface Arctic prokaryotes. *Environ. Microbiol.* **2008**, *10*, 2444–2454. [CrossRef]

53. Caputi, S.S.; Careddu, G.; Calizza, E.; Fiorentino, F.; Maccapan, D.; Rossi, L.; Costantini, M.L. Seasonal Food Web Dynamics in the Antarctic Benthos of Tethys Bay (Ross Sea): Implications for Biodiversity Persistence Under Different Seasonal Sea-Ice Coverage. *Front. Mar. Sci.* **2020**, *7*, 594454. [CrossRef]
54. Cantero, L.P.; Boero, F.; Piraino, S. Shallow-water benthic hydroids from Tethys Bay (Terra Nova Bay, Ross Sea, Antarctica). *Polar Biol.* **2013**, *36*, 731–753. [CrossRef]
55. Calizza, E.; Rossi, L.; Careddu, G.; Caputi, S.S.; Costantini, M.L. Species richness and vulnerability to disturbance propagation in real food webs. *Sci. Rep.* **2019**, *9*, 19331. [CrossRef] [PubMed]
56. Michel, L.N.; Danis, B.; Dubois, P.; Eleaume, M.; Fournier, J.; Gallut, C.; Jane, P.; Lepoint, G. Increased sea ice cover alters food web structure in East Antarctica. *Sci. Rep.* **2019**, *9*, 8062. [CrossRef]
57. Clark, G.F.; Stark, J.S.; Palmer, A.S.; Riddle, M.J.; Johnston, E.L. The Roles of Sea-Ice, Light and Sedimentation in Structuring Shallow Antarctic Benthic Communities. *PLoS ONE* **2017**, *12*, e0168391. [CrossRef] [PubMed]
58. Pearse, J.S.; McClintock, J.B.; Bosch, I. Reproduction of Antarctic Benthic Marine Invertebrates: Tempos, Modes, and Timing. *Am. Zoöl.* **1991**, *31*, 65–80. [CrossRef]
59. Hayward, P.J. *Antarctic Chilostomatus Bryozoa*; Oxford University Press Inc.: New York, NY, USA, 1995; p. 355.
60. Kuklinski, P. Atlas of Antarctic Bryozoa. Available online: http://www.iopan.gda.pl/ekologia/Antarctica/index.php (accessed on 1 May 2017).
61. Morrissey, J.H. Silver stain for proteins in polyacrylamide gels: A modified procedure with enhanced uniform sensitivity. *Anal. Biochem.* **1981**, *117*, 307–310. [CrossRef]
62. Mouchi, V.; Lartaud, F.; Guichard, N.; Immel, F.; de Rafélis, M.; Broussard, C.; Crowley, Q.G.; Marin, F. Chalky versus foliated: A discriminant immunogold labelling of shell microstructures in the edible oyster *Crassostrea gigas*. *Mar. Biol.* **2016**, *163*, 256. [CrossRef]
63. Beasley, M.M.; Bartelink, E.J.; Taylor, L.; Miller, R.M. Comparison of transmission FTIR, ATR, and DRIFT spectra: Implications for assessment of bone bioapatite diagenesis. *J. Archaeol. Sci.* **2014**, *46*, 16–22. [CrossRef]
64. Dauphin, Y. Comparative studies of skeletal soluble matrices from some Scleractinian corals and Molluscs. *Int. J. Biol. Macromol.* **2001**, *28*, 293–304. [CrossRef] [PubMed]
65. Kanold, J.M.; Guichard, N.; Immel, F.; Plasseraud, L.; Corneillat, M.; Alcaraz, G.; Brümmer, F.; Marin, F. Spine and test skeletal matrices of the Mediterranean sea urchin *Arbacia lixula*—A comparative characterization of their sugar signature. *FEBS J.* **2015**, *282*, 1891–1905. [CrossRef] [PubMed]
66. Immel, F.; Broussard, C.; Catherinet, B.; Plasseraud, L.; Alcaraz, G.; Bundeleva, I.; Marin, F. The Shell of the Invasive Bivalve Species Dreissena polymorpha: Biochemical, Elemental and Textural Investigations. *PLoS ONE* **2016**, *11*, e0154264. [CrossRef]
67. Coplen, T.B. Guidelines and recommended terms for expression of stable-isotope-ratio and gas-ratio measurement results. *Rapid Commun. Mass Spectrom.* **2011**, *25*, 2538–2560. [CrossRef]
68. Brand, W.A.; Coplen, T.B.; Vogl, J.; Rosner, M.; Prohaska, T. Assessment of international reference materials for isotope-ratio analysis (IUPAC Technical Report). *Pure Appl. Chem.* **2014**, *86*, 425–467. [CrossRef]
69. van Geldern, R.; Barth, J.A. Optimization of instrument setup and post-run corrections for oxygen and hydrogen stable isotope measurements of water by isotope ratio infrared spectroscopy (IRIS). *Limnol. Oceanogr. Methods* **2012**, *10*, 1024–1036. [CrossRef]
70. van Geldern, R.; Schulte, P.; Mader, M.; Baier, A.; Barth, J.A.C. Spatial and temporal variations of pCO_2, dissolved inorganic carbon and stable isotopes along a temperate karstic watercourse. *Hydrol. Process.* **2015**, *29*, 3423–3440. [CrossRef]
71. Cheng, L.; Normandeau, C.; Bowden, R.; Doucett, R.; Gallagher, B.; Gillikin, D.P.; Kumamoto, Y.; McKay, J.L.; Middlestead, P.; Ninnemann, U.; et al. An international intercomparison of stable carbon isotope composition measurements of dissolved inorganic carbon in seawater. *Limnol. Oceanogr. Methods* **2019**, *17*, 200–209. [CrossRef]
72. Barnes, D.K.; Ireland, L.; Hogg, O.T.; Morely, S.; Enederlein, P.; Sands, C.J. Why is the Southern Orkney Isalnd shelf (the world's first high seas marine protected area) a carbon immobilization hotspot? *Glob. Chang. Biol.* **2016**, *22*, 1110–1120. [CrossRef]
73. Key, M.M.; Rossi, R.K.; Smith, A.M.; Hageman, S.J.; Patterson, W.P. Stable isotope profiles of skeletal carbonate validate annually-produced growth checks in the bryozoan *Melicerita chathamensis* from Snares Platform, New Zealand. *Bull. Mar. Sci.* **2018**, *94*, 1447–1464. [CrossRef]
74. Lombardi, C.; Gambi, M.C.; Vasapollo, C.; Taylor, P.; Cocito, S. Skeletal alterations and polymorphism in a Mediterranean bryozoan at natural CO_2 vents. *Zoomorphology* **2011**, *130*, 135–145. [CrossRef]
75. Lombardi, C.; Cocito, S.; Gambi, M.C.; Taylor, P.D. Morphological plasticity in a calcifying modular organism: Evidence from an *in situ* transplant experiment in a natural CO_2 vent system. *R. Soc. Open Sci.* **2015**, *2*, 140413. [CrossRef]
76. Lombardi, C.; Taylor, P.D.; Cocito, S.; Bertolini, C.; Calosi, P. Low pH conditions impair module capacity to regenerate in a calcified colonial invertebrate, the bryozoan *Cryptosula pallasiana*. *Mar. Environ. Res.* **2017**, *125*, 110–117. [CrossRef]
77. Kuklinski, P.; Taylor, P.D. Mineralogy of Arctic bryozoan skeletons in a global context. *Facies* **2009**, *55*, 489–500. [CrossRef]
78. Krzeminska, M.; Kuklinski, P.; Najorka, J.; Iglikowska, A. Skeletal Mineralogy Patterns of Antarctic Bryozoa. *J. Geol.* **2016**, *124*, 411–422. [CrossRef]
79. Smith, A.M.; Key, M.M.; Gordon, D.P. Skeletal mineralogy of bryozoans: Taxonomic and temporal patterns. *Earth-Sci. Rev.* **2006**, *78*, 287–306. [CrossRef]
80. Ciavatta Ml Lefranc, F.; Vieira, L.; Kiss, R.; Carbone, M.; van Otterlo, W.A.L.; Lopanik, N.B.; Waeshenback, A. The Phylum Bryozoa: From Biology to Biometical Potentia. *Mar. Drugs* **2020**, *18*, 200. [CrossRef]

81. Clamp, A.; Jayson, G. The clinical development of the bryostatins. *Anti-Cancer Drugs* **2002**, *13*, 673–683. [CrossRef]
82. Raghuvanshi, R.; Bharate, S.B. Preclinical and clinical studies on bryostains, a class of marine-derived protein kinase C modulators: A mini review. *Curr. Top. Med. Chem.* **2020**, *20*, 1124–1135. [CrossRef]
83. Ramos-Silva, P.; Marin, F.; Kaandorp, J.; Marie, B. Biomineralization toolkit: The importance of sample cleaning prior to the characterization of biomineral proteomes. *Proc. Natl. Acad. Sci. USA* **2013**, *110*, E2144–E2146. [CrossRef]
84. Weiner, S.; Traub, W. Macromolecules in mollusc shells and their functions in biomineralization. *Philos. Trans. R. Soc. London B Biol. Sci.* **1984**, *304*, 425–434. [CrossRef]
85. Marin, F.; Marie, B.; Hamada, S.B.; Silva, P.; Le Roy, N.; Guichard, N.; Wolf, S.; Montagnani, C.; Joubert, C.; Piquemal, D.; et al. Shellome: Proteins involved in molluscs shell biomineralization—Diversity, functions. In *Recent Advances in Pearl Research*; Terra Pub: San Francisco, CA, USA, 2013; pp. 149–168.
86. Osuna-Mascaró, A.; Cruz-Bustos, T.; Benhamada, S.; Guichard, N.; Marie, B.; Plasseraud, L.; Corneillat, M.; Alcaraz, G.; Checa, A.; Marin, F. The shell organic matrix of the crossed lamellar queen conch shell (*Strombus gigas*). *Comp. Biochem. Physiol. Part B (Biochem. Mol. Biol.)* **2014**, *168*, 76–85. [CrossRef] [PubMed]
87. Marin, F.; Luquet, G. Unusually acidic proteins in biomineralization. In *Handbook of Biomineralization: Biological Aspects and Structure Formation*; Wiley: Hoboken, NJ, USA, 2007; pp. 273–290.
88. Hunt, S. Scleroprotein and chitin in the exoskeleton of the ectoproct *Flustra foliacea*. *Comp. Biochem. Physiol.* **1972**, *43*, 571–574. [CrossRef]
89. Kaya, M.; Baublys, V.; Šatkauskienė, I.; Akyuz, B.; Bulut, E.; Tubelytė, V. First chitin extraction from *Plumatella repens* (Bryozoa) with comparison to chitins of insect and fungal origin. *Int. J. Biol. Macromol.* **2015**, *79*, 126–132. [CrossRef]
90. Goffinet, G.; Jeuniaux, C. Distribution et importance quantitative de la chitine dans les coquilles de mollusques. *Cah. Biol. Mar.* **1979**, *20*, 341–349.
91. Furuhashi, T.; Schwarzinger, C.; Miksik, I.; Smrz, M.; Beran, A. Molluscan shell evolution with review of shell calcification hypothesis. *Comp. Biochem. Physiol. Part B Biochem. Mol. Biol.* **2009**, *154*, 351–371. [CrossRef]
92. Oudot, M.; Neige, P.; Ben Shir, I.; Schmidt, A.; Strugnell, J.M.; Plasseraud, L.; Broussard, C.; Hoffmann, R.; Lukeneder, A.; Marin, F. The shell matrix and microstructure of the Ram's Horn squid: Molecular and structural characterization. *J. Struct. Biol.* **2020**, *211*, 107507. [CrossRef]
93. Agbaje, O.B.A.; Ben Shir, I.; Zax, D.B.; Schmidt, A.; Jacob, D.E. Biomacromolecules within bivalve shells: Is chitin abundant? *Acta Biomater.* **2018**, *80*, 176–187. [CrossRef] [PubMed]
94. Dini, M.; Stenni, B. Oxygen isotope characterization of Terra Nova Bay seawater. In *Ross Sea Ecology*; Faranda, F., Guglielmo, L., Ianora, A., Eds.; Springer: Berlin/Heidelberg, Germany, 2000; Chapter 3; pp. 27–37.
95. Jacobs, S.S.; Giulivi, C.F.; Mele, P.A. Freshening of the Ross Sea During the Late 20th Century. *Science* **2002**, *297*, 386–389. [CrossRef] [PubMed]